

Collective locomotion of two-dimensional lattices of flapping plates

Silas Alben*

*Department of Mathematics, University of Michigan, Ann Arbor, MI 48109, USA**

(Dated: July 29, 2020)

We study the propulsive properties of rectangular and rhombic lattices of flapping plates at $O(10-100)$ Reynolds numbers in incompressible flow. Here the fluid dynamics often converge to time-periodic in 5-30 flapping periods, facilitating accurate computations of time-averaged thrust force and input power. We classify the propulsive performances of the lattices and the periodicity of the flows in a space of five parameters: flapping amplitude, frequency (or Reynolds number), horizontal and vertical spacings between plates, and oncoming fluid stream velocity. Nonperiodic states are most common at small streamwise spacing, large lateral spacing, and large Reynolds number.

Lattices that are closely spaced in the streamwise direction produce intense vortex dipoles between adjacent plates. The lattices transition sharply from drag- to thrust-producing as these dipoles switch from upstream to downstream orientations at critical flow speeds. Near these transitions the flows pass through a variety of periodic and nonperiodic states, with and without up-down symmetry, and multiple stable self-propelled speeds can occur. As the streamwise spacing increases (and with large lateral spacing), the plates may shed typical vortex wakes (e.g. reverse von Kármán streets) that impinge on downstream neighbors. The most efficient streamwise spacing increases with flapping amplitude. With small lateral spacing, the rectangular lattices have Poiseuille-type flows that yield net drag, while the rhombic lattices may shed vortices and generate net thrust, sometimes with relatively high efficiency. As lateral spacing increases to the vicinity of a plate length and beyond, the rectangular lattices begin to shed vortices and generate thrust, eventually with slightly higher efficiencies than the rhombic lattices, as the two types of lattice flows converge. At $Re = 70$, the lattices' maximum Froude efficiencies are about twice those of an isolated plate (only considering nearly periodic lattice flows). As Re decreases, the lattices' efficiency advantage increases; the lattices obtain net thrust (and self-propulsion) at lower Re than an isolated flapping plate does.

The mean input power needed to generate the lattice flows can be estimated in the limits of small and large streamwise spacings, with small-gap and Poiseuille-like flows between the plates respectively in the two cases. For both lattices, the mean input power saturates as the lateral spacing becomes large (and thrust occurs). At small lateral spacings, the rhombic lattices' input power may be much larger when the plates overlap, leading to a decrease in Froude efficiency.

*Electronic address: alben@umich.edu

I. INTRODUCTION

Propulsion by flapping foils has garnered considerable interest in recent years, as a bio-inspired alternative to traditional designs for aquatic and aerial vehicles. Flapping propulsion has potential advantages in efficiency, maneuverability, and stealth, particularly at small and medium scales [1–12]. Some of the different types of flapping bodies and motions considered are: rigid or flexible foils [1, 2, 4, 9] undergoing heaving and/or pitching motions [7, 8, 12–15]; flexible foils oscillated at one point and otherwise bending passively [16–21], or with an internal driving force distributed all along the foil [22, 23]; foils oscillated transversely to an imposed oncoming flow [4, 7], or swimming (translating/rotating) freely under a force balance law [19, 24–27]. Another large body of work has considered the stability and dynamics of passive flexible flags, plates, and membranes in fluid flows [28]. A common way to understand the physics of force generation by flapping foils is to relate the forces on the foil to the vorticity shedding patterns, often von Kármán vortex streets or other ordered arrays. Given a certain body motion, the formation of such vorticity distributions depends on unsteady large-scale boundary layer separation and is difficult to describe with a simple analytical approach. Computational and experimental approaches are more commonly used to describe the phenomena. Several works have found that Froude efficiency is maximized when a reverse von Kármán street is formed, typically near Strouhal numbers of 0.2–0.5 for biological and biomimetic swimmers [4, 8, 29–34]. Outside this range, other ordered and disordered vortex wakes are observed [8, 35, 36].

A number of works have extended the study to the case of multiple flapping foils interacting in a fluid [37–42]. Key parameters are the phase differences between the foils’ oscillations, and the spacings (in-line and/or transverse) between the foils. If one body interacts with a typical vortex wake of another (e.g. an inverse von Kármán street), the spacings and phasings will largely determine the types of vortex-body collisions that occur and the resulting forces. Vortices impinging on foils alter the pressure distribution and vortex shedding at the leading and trailing edges [38, 43]. The vortex wakes may be strengthened or weakened through the interactions, with the possibility of increased thrust or efficiency in some cases [8]. Related lines of work have addressed interactions between a single body and ambient vorticity (e.g. shed from a static obstacle) [10, 44–49], vortex-wall collisions [50–55], and interactions between multiple passive flapping flags and plates [56–60]. Although much is known, the complicated physics of vortex shedding remains an obstacle to a simple quantitative description of multiple-body/body-vortex interaction problems [61, 62]. Even the apparently simpler case of collective interactions in the zero Reynolds number limit [63–68], with linear flow equations but geometrical complexities, has many open issues, among them close interactions between bodies [69, 70].

When multiple bodies are considered, the number of degrees of freedom increases enormously even with many simplifying assumptions. We now have to choose a particular geometry and kinematics for each body (including relative phases for periodic motions). We need to resolve the flow on a wide range of scales simultaneously, from the size of a large group of bodies and their vortex wakes to the scale of thin, time-dependent boundary layers and separation regions on each body surface. For prescribed spatial configurations of the bodies, there are many possible choices. A potential way to simplify the problem is to allow a group of bodies to evolve dynamically and look for configurations that are attracting states of various initial conditions [62, 71–79]. Many of these involve quantized spacings that are related to the natural spacings of vortex streets. If the spatial configuration evolves dynamically

according to the forces on the bodies, the nonlinear dynamics are generally sensitive to initial conditions as well as the details of close interactions and/or collisions between bodies. It is very difficult to classify the whole range of possibilities in such systems. Many studies have instead focused on configurations seen in groups of biological organisms [38, 45, 80–91]. Other recent studies have used machine learning to determine optimal motions of groups of swimmers [92, 93]. Another large body of work concerns the use of simplified laws of interaction in place of detailed fluid dynamics, to model schools and flocks of bodies [94, 95].

Following previous models [78, 79, 96], experiments [71, 72, 97], and simulations [25, 98–102] inspired by biology [103], we consider a particular version of the multiple flapping foil problem, with simple body geometries and kinematics, that is amenable to a wide (though by no means exhaustive) exploration of parameter space: thin plates that are oscillated vertically and moved horizontally together through a viscous fluid. The plates and motions considered here are fore-aft symmetric for simplicity; adding a pitching motion [26], an asymmetric body thickness profile [99], and/or active and/or passive deformations [73, 93] can enhance the thrust generated and the propulsive efficiency. The main quantities of interest are the time-averaged horizontal force (i.e. thrust or drag) and the input power needed to oscillate the plates vertically in the fluid. We study perhaps the most common measure of efficiency, the Froude (propeller) efficiency, a ratio of average propulsive power to average input power required to oscillate the foils [1, 4]. We also study an alternative output quantity, the self-propelled speed(s) of the foils [25, 27, 73, 93, 97].

II. MODEL

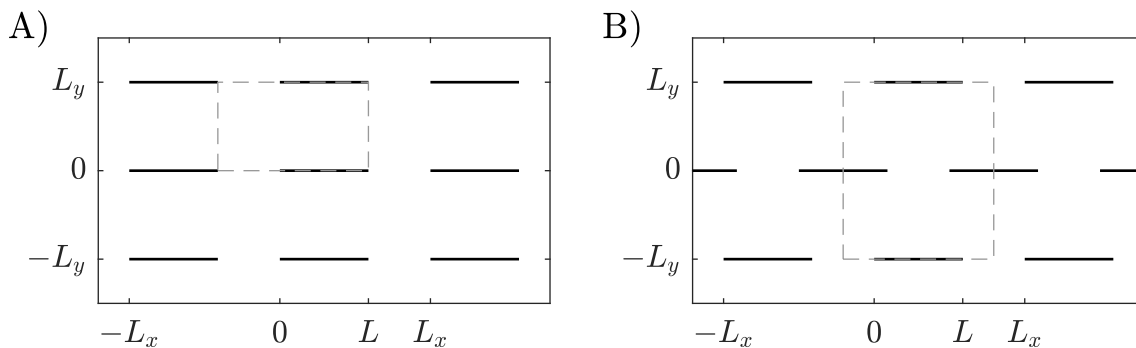


FIG. 1: A) A rectangular lattice of plates. An L_x -by- L_y unit cell is shown with a dashed outline. B) A rhombic lattice of plates. An L_x -by- $2L_y$ double unit cell is shown with a dashed outline.

We consider a lattice of plates (rectangular or rhombic, shown in figure 1), each plate moving with the same velocity $\mathbf{U}(t) = (U, V(t))$, constant in the horizontal direction, and sinusoidal in the vertical direction:

$$\frac{V(t)}{fL} = 2\pi \frac{A}{L} \sin(2\pi t) \left(1 - e^{-(t/t_0)^2}\right), \quad (1)$$

with A the amplitude and f the frequency of the vertical displacement corresponding to $V(t)$. The exponential term allows smooth start-up from rest with time constant $t_0 = 0.2$ (the particular value is not important, as our focus is on

the eventual steady state behavior). We nondimensionalize quantities using the plate length L as the characteristic length, the flapping period $1/f$ as the characteristic time, and the fluid mass density ρ_f as the characteristic mass density.

We solve the incompressible Navier-Stokes equations, nondimensionalized, in the rest frame of the lattice [104]:

$$\partial_t \mathbf{u} + \mathbf{u} \cdot \nabla \mathbf{u} = -\nabla p + \frac{1}{\text{Re}_f} \nabla^2 \mathbf{u} - \frac{d\mathbf{U}}{dt}(t), \quad (2)$$

$$\nabla \cdot \mathbf{u} = 0. \quad (3)$$

The basic dimensionless parameters are

$$\frac{A}{L}, \text{Re}_f = \frac{fL^2}{\nu}, l_x = \frac{L_x}{L}, l_y = \frac{L_y}{L}, U_L = \frac{U}{fL}, \quad (4)$$

where ν is the kinematic viscosity of the fluid and L_x and L_y are the lattice spacings in the x and y directions, respectively. Other important dimensionless parameters, combinations of those above, are:

$$\text{Re} = \frac{4AfL}{\nu}, \text{Re}_U = \frac{UL}{\nu}, U_A = \frac{U}{fA}, \text{St} = \frac{2}{U_A}. \quad (5)$$

Re is the Reynolds number based on the mean vertical velocity of the foil on each half-stroke, and is therefore a better measure of the ratio of inertial to viscous forces than Re_f , which we think of as a dimensionless frequency. It is convenient for computations to nondimensionalize time by the flapping period, but the flapping frequency is one of the kinematic parameters we vary as we search for optimal flapping kinematics as well as plate spacings. Therefore, for comparison across kinematic parameters, Re_U gives a more uniform measure of the horizontal speed of the foil than U_L (since L and ν are considered fixed in all cases, while f varies). To find the horizontal velocities that yield efficient thrust-generating states and self-propelled states, previous work has shown that we should search in certain ranges of St (or U_A , twice its reciprocal) [4, 8, 29–34].

Instead of prescribing the horizontal velocity U_L , one can allow it to evolve dynamically according to Newton’s second law, setting the plates’ rate of change of horizontal momentum equal to the horizontal component of the net fluid forces on them [25–27, 73, 100]. In this case, we have the plates’ dimensionless mass M as a control parameter instead of U_L . We have simulated this case, with $U_L(t)$ “free” and M fixed, and the case of fixed U_L , and in both cases, periodic and nonperiodic flow dynamics can arise generically at different parameters. The coupling of body and fluid motion seems to add some additional complexity to the problem, so here we focus on the case with fixed U_L , which is also the focus of most previous flapping foil studies, including those that investigated Froude efficiency [1, 4, 6, 29]. The case with fixed U_L and zero time-averaged thrust corresponds to the large-mass limit of cases with time-varying U_L —those with initial conditions such that the fixed value of U_L is an attracting state.

The flow starts at rest, and evolves until it converges to a periodic steady state, or remains nonperiodic up to a chosen end time of a simulation (typically $t = 15$ or 30). Some of these nonperiodic states may eventually converge to periodic in longer simulations. However, most have irregular oscillatory behaviors and seem likely to remain nonperiodic. These cases seem to require much longer simulations to precisely compute the long-time averages of fluid forces and input power. Thus we mostly focus on the parameters that yield a periodic state, generally those at lower Reynolds numbers, but give information about nonperiodic results in some cases.

For a plate with zero thickness in a viscous flow, the pressure and viscous shear stress diverge near the plate tips as the inverse square root of distance [105, 106]. In the limit of zero plate thickness, the contribution of the pressure on the plate edges to the net horizontal force is zero. The net horizontal force on the plate is due only to the viscous shear stress on the two sides of the plate,

$$F_x = \frac{1}{\text{Re}_f} \int_0^1 [\partial_y u(x, 0, t)]_{-}^{+} dx. \quad (6)$$

The bracket notation denotes the jump in $\partial_y u$ along the plate (the value at the top minus the value at the bottom). The vertical force is due to the pressure difference across the plate:

$$F_y = \int_0^1 -[p(x, 0, t)]_{-}^{+} dx. \quad (7)$$

Important related quantities are the input power $P_{in}(t)$ and the Froude efficiency η_{Fr} :

$$P_{in}(t) = \frac{V(t)}{fL} F_y; \quad \tilde{P}_{in}(t) = \text{Re}_f^3 P_{in}(t); \quad \eta_{Fr} = \frac{U \langle F_x(t) \rangle}{\langle P_{in}(t) \rangle}. \quad (8)$$

Here $\tilde{P}_{in}(t)$ is the input power nondimensionalized with ν/L^2 in place of f , for comparison across cases with different f (since L and ν are assumed fixed). The numerator and denominator of η_{Fr} both acquire factors of Re_f^3 with the same change in nondimensionalization, resulting in no change for η_{Fr} .

Since ∇p in (2) is doubly periodic, it has a Fourier decomposition in which the mean (or constant part) has components we denote $\Delta p_x/l_x$ and $\Delta p_y/l_y$, and ∇p_1 is the remainder (the mean-zero part). Thus p is decomposed into mean-zero and linear terms:

$$p = p_1 + \frac{\Delta p_x}{l_x} x + \frac{\Delta p_y}{l_y} y. \quad (9)$$

p_1 is determined (up to a constant) by the incompressibility condition, $\nabla \cdot \mathbf{u} = 0$. The constant is fixed by setting p_1 to zero at an arbitrary point (e.g. the lower left corner of the flow domain). To fix the unknowns Δp_x and Δp_y , we impose a condition on the net fluid flow in the vertical and horizontal directions. We assume that the lattice of flapping plates is situated in a larger flow domain that ends at solid boundaries, where the flow is zero. We therefore assume that the spatially periodic flow approximates the flow away from the boundaries, but take the spatial average of the flow in the lattice to be zero at all times, to match that at the boundaries. The same assumption has been used in theoretical and computational studies of sedimenting suspensions at zero [107–115] and nonzero [116–119] Reynolds numbers, and with background turbulence [120]. In these studies the flow is typically solved in a periodic lattice or periodic cell domain, and the velocity of the sedimenting particles relative to zero-volume-flux axes is interpreted as the velocity in the physical or lab frame. In our case, the plates have zero volume, so the volume flux is that of the fluid alone. For periodic domain models of sedimentation and in the present work on flapping locomotion, there is assumed to be a transition region near the boundary where the flow deviates from spatially periodic, to obtain zero flow at the boundary. In a sedimentation simulation, Mucha *et al.* found that including the boundary region in the simulation had a negligible effect on particle velocity statistics far from the boundary [117].

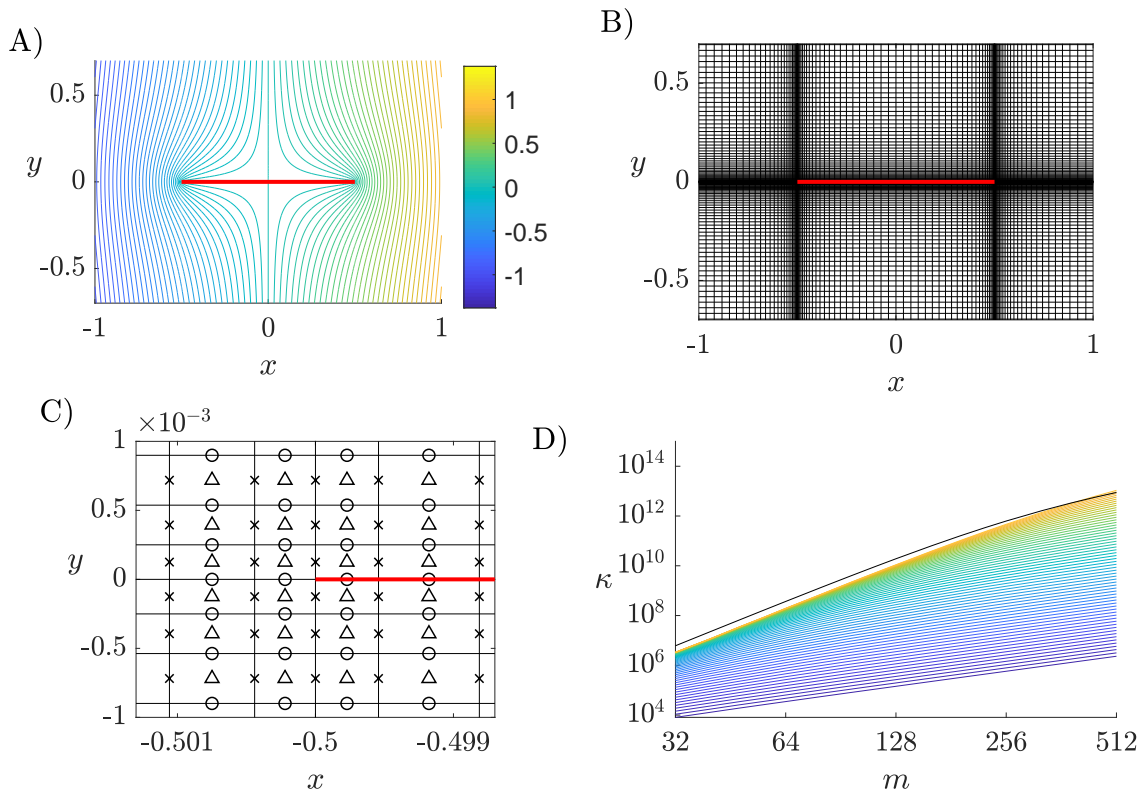


FIG. 2: Test problem and numerical grids. A) Streamlines for potential flow past a flat plate. B) Example of a grid with refinement near the plate (red). C) A close-up of the grid near the left plate edge. The values of the velocity components and pressure (u , v , and p) are solved at the locations of the crosses, circles, and triangles, respectively. D) The growth in the 2-norm condition number of the discrete Laplacian matrix. Each colored line plots the condition number versus m for a given η , ranging from $1 - 2^{-2}$ (darkest blue line) to $1 - 2^{-14}$ (lightest yellow line); $1 - \eta$ decreases by a factor of $2^{-0.2}$ from each line to the one above it, giving an increased concentration of points near the plate edges.

III. NUMERICAL METHOD

We choose a flat plate geometry instead of a thin curved body (e.g. an ellipse) because it fits a periodic rectilinear grid, at the expense of creating flow singularities at the plates' edges. To study the effect of the singularity on a finite-difference solution of (2)–(3), we study a simpler model problem with the same type of singularity: potential flow past a flat plate, shown in figure 2A. The plate is the red line segment—extending along $(-1/2 \leq x \leq 1/2; y = 0)$ —and the complex potential is $w(z) = \sqrt{1/4 - z^2}$, with branch cut lying along the plate. We solve Laplace's equation for the stream function $\psi = \text{Im}\{w\}$ in a rectangle R centered at the origin (the plate center), with lengths 3 and 2 in the x and y directions, respectively:

$$\nabla^2 \psi = 0 \quad , \quad (x, y) \in R : -3/2 \leq x \leq 3/2, -1 \leq y \leq 1; \quad (10)$$

$$\psi = 0 \quad , \quad -1/2 \leq x \leq 1/2, y = 0; \quad (11)$$

$$\psi = \text{Im}\{\sqrt{1/4 - (x + iy)^2}\} \quad , \quad (x, y) \in \partial R. \quad (12)$$

ψ is continuous but its first derivatives diverge as inverse square roots of distance from the plate edges. Based on Stokes-flow solutions and local asymptotics of Navier-Stokes solutions [105, 106], ψ has the same type of singularity as the velocity components in (2)–(3) (i.e. the *viscous* flows, not the potential flow defined by ψ). Both $\nabla^2\psi$ and the highest-order derivatives in (2)–(3), i.e. ∇^2u , ∇^2v , and ∇p , diverge as distance from the plate edges to the $-3/2$ -power. We will use second-order finite differences to discretize both the test problem (10) and the viscous problem (2)–(3), even though the Taylor series expansions underlying the finite difference approximations diverge at the plate edges. Our goal with the test problem is to measure the error in a case with a simple analytical solution, given by (12) in all of R .

To mitigate the errors, we will employ nonuniform rectilinear (tensor-product) grids, and concentrate grid points near the plate edges, and along the plate surfaces, as shown in figure 2B. For the viscous problem, we use the MAC (marker-and-cell) scheme for incompressible flows [121] with the grid aligned with the plate as shown in the sample grid in figure 2C. The velocity components u and v are solved at the crosses and circles respectively, and the pressure p is solved at the triangles. The x and y locations of the symbols are either on the grid lines, or at midpoints between grid lines. For the test problem, we solve ψ on the u -grid in panel C (i.e. at the crosses).

The grid lines are defined from uniform grids using a grid-stretching parameter η . For the x -grid on the plate in panels B and C, we first define a uniform grid from $-1/2$ to $1/2$ in X , and then the x coordinates of the grid are defined by:

$$x = X + \eta \frac{1}{2\pi} \sin 2\pi X, \quad -1/2 \leq X \leq 1/2. \quad (13)$$

If the uniform grid spacing in X is ΔX , the spacing Δx on the stretched grid x increases from approximately $1 - \eta$ at the plate edges to $1 + \eta$ at the plate center. As η increases from 0 to 1, the stretched grid transitions from uniform to highly concentrated at the plate edges. We choose a number of grid points for the plate, and then for the x -grid to the left and right of the plate in panel B, we set the number of grid points to be approximately that in the grid along the plate, scaled by the ratio of the outer region length to the plate length (unity), raised to the $1/2$ power. The functional form of the grids is the same as that in (13), with a stretching factor chosen so that the grid density is approximately continuous at the plate edges. The y grid is defined similarly to (13),

$$y = Y - \eta \frac{l_y}{2\pi} \sin 2\pi Y/l_y, \quad -l_y/2 \leq Y \leq l_y/2, \quad (14)$$

given a uniform grid in Y . In the viscous computations that follow, the total numbers of grid points in x and y are similar (within a factor of 2), and in the potential flow test problem here they are equal (and denoted m). For the test problem, we solve (10) on the grid shown by crosses in figure 2B, for various values of m and η . Due to the discontinuity in flow quantities (e.g. velocity derivatives and pressure) across the plate, we use one-sided finite differences near the plate for all derivatives in both the test problem and the viscous solver, to maintain their accuracy away from the plate edges. To describe when the accuracy becomes hampered by ill-conditioning, we present the 2-norm condition number of the discrete Laplacian matrix for ψ , for various m and η in figure 2D. Each colored line plots the condition number versus m for a given η , ranging from $1 - 2^{-2}$ (i.e. 0.75, darkest blue line) to $1 - 2^{-14}$ (lightest yellow line), in order of increasing concentration of points near the plate edges. For each η , the condition

number initially grows faster than m^{-2} , then asymptotes to this scaling for sufficiently large m . The m at which the transition occurs depends on η . For $\eta = 0.75$ (darkest blue line), the line scales as m^{-2} for all $m \geq 32$, while for $\eta = 1 - 2^{-14}$ (lightest yellow line), the transition is only beginning to occur at $m = 512$. For a given η , when m is relatively small, increasing m increases the density of points near the plate edges more than in the rest of the domain. When m is sufficiently large, further increases in m increase the density of points by the same percentage everywhere. At this point we obtain the usual m^{-2} condition number scaling of the discrete Laplacian, albeit with a non-uniform grid. For $m \leq 512$ and $\eta \leq 1 - 2^{-14}$, the condition number indicates a round-off error at least a few orders of magnitude below double precision (10^{-16}). In the viscous simulations, we set $\eta = 0.95$, corresponding to a line in the bottom fifth of those in panel D, and the round-off error is several orders of magnitude away from double precision.

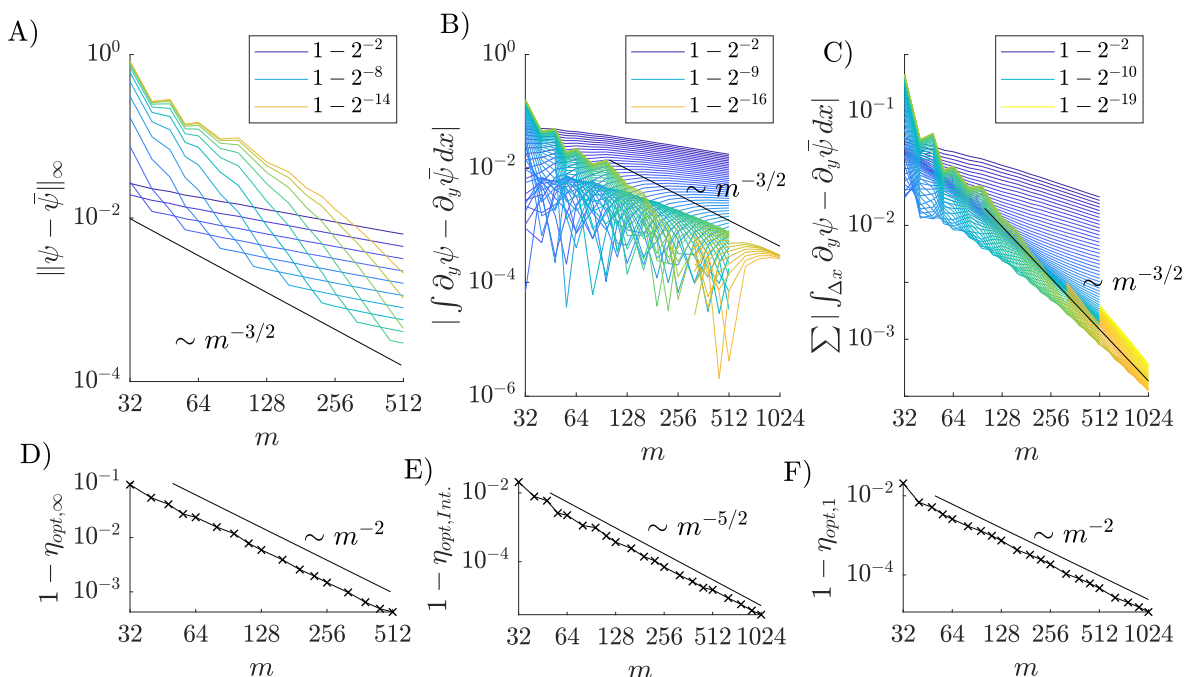


FIG. 3: Errors in the computed potential flow stream function relative to the exact solution. A) Infinity (sup) norm error over the 3-by-2 rectangular domain. B) Error in integral of $\partial_y \psi$ over the top left half of the plate. C) Sum of the absolute values of the errors in $\partial_y \psi$, at the midpoints of each grid subinterval on the top left half of the plate. D) and F) For each m , the values of η at which the minimum errors occur in panels A and C. E) the values of η corresponding to the envelope below the black fit line in panel B.

We now study the effects of m and η on errors for the test problem, where the analytical solution is known. In figure 3A-C, we plot a few different measures of error in ψ . Panel A shows the infinity (sup) norm of the error in the computed ψ over the full grid relative to the exact solution $\bar{\psi}$, given by (12) in all of R . Each colored line again corresponds to a particular η value, a few of which are labeled in the legend (the remaining values lie between these values, and are of the form $1 - 2^{-k/5}$ for $k = 10, 11, \dots, 69, 70$). For each line, the error initially decreases rapidly with increasing m , then much more slowly (as $m^{-1/2}$) for further increases in m . This transition again reflects the

transition in where the density of points is being increased most, near the tip at smaller m , and uniformly at large m . The singularity at the plate edges reduces the scaling from m^{-2} for a smooth problem with second-order finite differences to $m^{-1/2}$. However, by choosing the best η for a given m , we obtain the lower envelope of the lines in panel A, which has scaling $m^{-3/2}$, closer to the smooth case. In the viscous simulations, we need to compute the forces on the plate, which require integrating the pressure and velocity gradient, each with inverse-square-root singularities near the plate edges. For the test problem, $\partial_y\psi$ is the analog of the velocity gradient, with the same singularity strength. In panel B, we plot the error in its integral over the top left half of the plate, computed with second-order finite differences and then integrated using the trapezoidal rule. The exact integral is $1/2$. Each curve again corresponds to a given η , which we take to $1 - 2^{-16}$ now, closer to 1, to see the asymptotic behavior at large m better. Each curve eventually scales as $m^{-1/2}$, but by taking the minimum error over η at a given m , we can do much better. In fact, for each m there is apparently an η for which the error passes through zero, as shown by the downward spikes of the curves on this log scale. The typical error magnitude in the vicinity of this η is shown by the upper envelope of the curves at somewhat larger m . The black fit line shows that this envelope scales as $m^{-3/2}$. Therefore, the error in the integral of $\partial_y\psi$ up to the plate edge behaves similarly to the maximum error in ψ over the domain. The error according to a somewhat more stringent criterion is shown in panel C. We again consider the integrated error in $\partial_y\psi$, but now integrate the absolute value of the error over the top left half of the plate. This avoids the cancellation of errors over different portions of the plate, which led to the error passing through zero in panel B. Therefore this measure of error avoids the possibility of errors being hidden by cancellation. If we compute it using the trapezoidal rule, the error is $+\infty$ in each case, because of the infinite value of $\partial_y\bar{\psi}$ at the plate edge. Therefore we use a version of the midpoint rule. On each grid interval on the top left half of the plate, we take the average of the computed values at the endpoint minus the exact value at the midpoint (which is always finite), and sum the absolute value of the difference, weighted by the length of each interval. The behavior is similar to that of panel A: for a fixed curve (fixed η), the error $\sim m^{-1/2}$ at large enough m . But the lower envelope of the curves $\sim m^{-3/2}$. Panels D–F show, for each m , the η values corresponding to the aforementioned envelopes. In panels A and C, these are the error-minimizing η at each m . Their distance from 1 is seen to decay as m^{-2} . In panel B, these are the η corresponding to the envelope, and here $1 - \eta$ decays slightly faster, approximately as $m^{-5/2}$.

Figure 3 shows that even with the plate edge singularities, errors can be decreased below 1% with m not very large ≈ 100 and η close to 1. For the viscous simulations, we have the additional need to resolve vorticity throughout the flow domain, though it is strongest near the plate edges. We set η to 0.95, close enough to 1 to greatly diminish errors at the plate edges, but far enough to avoid the possibility of ill-conditioning in the viscous system of equations. We take m between 256 to 512, and find that these choices are sufficient to resolve the flows and fluid forces on the plate to within a few percent in relative error for the ranges of parameters (e.g. domain size, Reynolds number, etc.) studied.

IV. SINGLE FLAPPING PLATE

Before studying lattices of flapping plates, we examine a single flapping plate in flows of various speeds to establish a baseline of performance to which the lattice configurations can be compared. We solve the second-order finite difference discretization of (2)–(3) on the MAC grid (e.g. figure 2B and C) as a fully coupled system for u , v , and p . To simulate an isolated flapping plate in an unbounded fluid, we employ upstream, downstream, and sidewall boundary conditions in the rectangular domain, and take the boundaries sufficiently far from the body that they affect the results by less than a few percent in relative error. The upstream and downstream sides are 3 and 8 plate lengths from the plate’s leading edge, and the sidewalls are 5 plate lengths from the plate. At the upstream boundary, $u = -U$ and $v = -V(t)$ are imposed. On the sidewalls, free-slip conditions are imposed ($\partial_y u = 0$, $v = -V(t)$) to avoid vorticity generation. At the downstream boundary, advective outflow conditions are used ($\partial_t u - \mathbf{U}(t) \cdot \nabla u = \partial_t v - \mathbf{U}(t) \cdot \nabla v = 0$). Similar boundary conditions have been used in other recent simulations of flows past bodies [122–126].

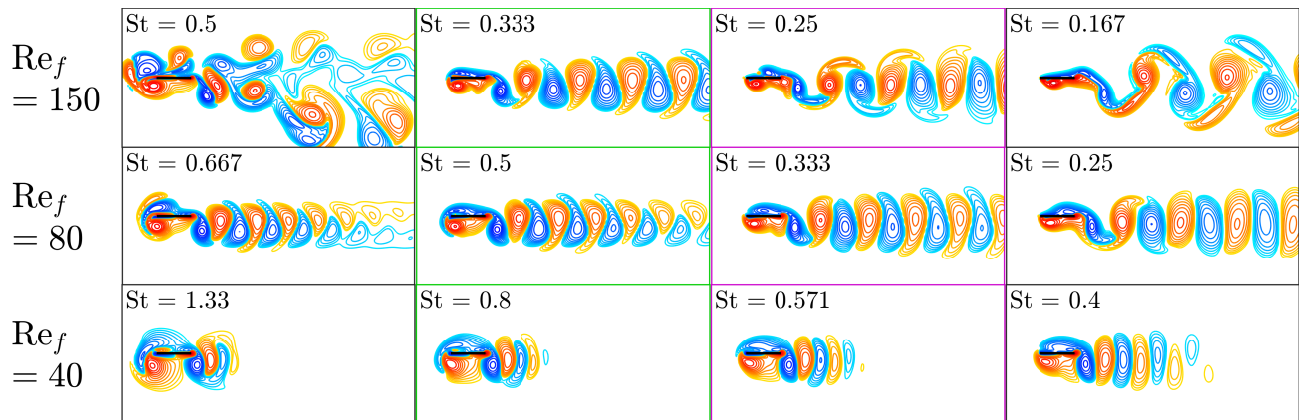


FIG. 4: Snapshots of vorticity fields with normalized amplitude $A/L = 0.2$ and different flapping frequencies (Re_f , labeled at left) and Strouhal numbers $St = 2Af/U$, labeled in each box, corresponding to increasing oncoming flow speed from left to right.

For an isolated body we have $l_x, l_y \rightarrow \infty$ in (4), and we are left with three parameters, A/L , Re_f , and St . Examples of flows with normalized flapping amplitude $A/L = 0.2$ and various Re_f and St are shown in figure 4. At zero oncoming flow speed, or infinite St (not shown), the flow has a left-right symmetric equilibrium state (with equal and opposite vorticity at the two plate edges). This state becomes unstable to asymmetric motions above a critical value of $Re = 4ARe_f/L$ ([24, 100]). For small but nonzero oncoming flow speed, and sufficiently large Re_f , the vortices shed from the plate edges collide with the body and may travel to the sidewall or upstream boundaries (violating the boundary conditions there). In the upper left panel of figure 4 ($Re_f = 150$, $St = 0.5$), however, the flow speed is sufficiently large that the vortex wake is generally advected downstream, and is a somewhat disordered array of dipoles, one shed per half-cycle. Moving one panel to the right (green box in the second column) is a smaller St value, close to where the Froude efficiency is maximized for this Re_f , and the larger oncoming flow allows the vortex wake

to organize into the familiar reverse von Kármán street [8]. One panel further to the right (purple box in the third column of the top row) is St close to the self-propelled state, where $\langle F_x \rangle = 0$. In the last column, the flow speed is much larger and the body experiences drag although the wake still resembles a reverse von Kármán street, but with more widely spaced vortices. The second and third rows show the same sequences of flows as oncoming flow speed is increased, but at successively smaller Re_f . Viscous diffusion of vorticity is more apparent, particularly in the bottom row. In the bottom two rows, the negative (blue) vortices move upwards relative to the positive (red) vortices at larger oncoming flow speeds, indicating the transition from reverse towards regular von Kármán streets [35]. For fish and birds at $Re = 10^3 - 10^5$, the optimally efficient St are generally in the range 0.2–0.4 [8], while here $Re = 10 - 10^2$, and the most efficient St are higher. The St that are close to optimal for Froude efficiency (green boxes) increase as Re decreases (from top to bottom rows), which is also seen in organisms as Re decreases [34].

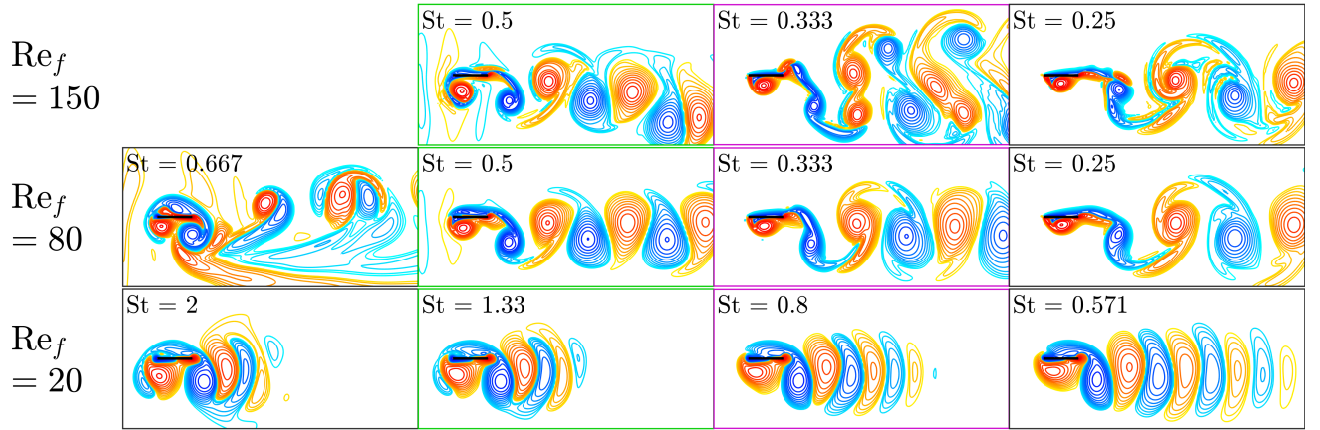


FIG. 5: Snapshots of vorticity fields with normalized amplitude $A/L = 0.4$ and other quantities as described in figure 4.

Figure 5 shows the same transitions with increases in oncoming flow speed, but with A/L increased to 0.4. At the upper left, no flow is shown, because at small flow speeds, vortices collide with the sidewalls. Moving rightward to the green box in the top row, we obtain an up-down asymmetric vortex street and vortex pairing, corresponding generally to nonzero average vertical force on the plate. The approximate self-propelled state (purple box) has an irregular vortex street with multiple vortices shed per half stroke, akin to the 2P wake [36]. At $Re_f = 80$ (second row), at the slowest speed ($St = 0.667$), the vortex wake again has a complicated structure. At St near the maximum efficiency state (0.5, green box), the wake is a reverse von Kármán street, which is maintained but dilated downstream at higher oncoming flow speeds. In the third row ($Re_f = 20$), the vortex street has the reverse von Kármán structure at all St shown. In general, the effect of increasing A/L to 0.4 is to increase the lateral spacing of the vortex street in the most efficient and self-propelled states (green and purple boxes). The horizontal spacing is influenced most directly by the oncoming flow speed, but A/L also plays a role in the timing of vortex formation and shedding.

In figure 6A, we plot the average horizontal force versus normalized oncoming flow speed for the six cases shown in figures 4 and 5. Values are omitted where the dynamics are non-periodic, which occurs over an interval of flow speeds

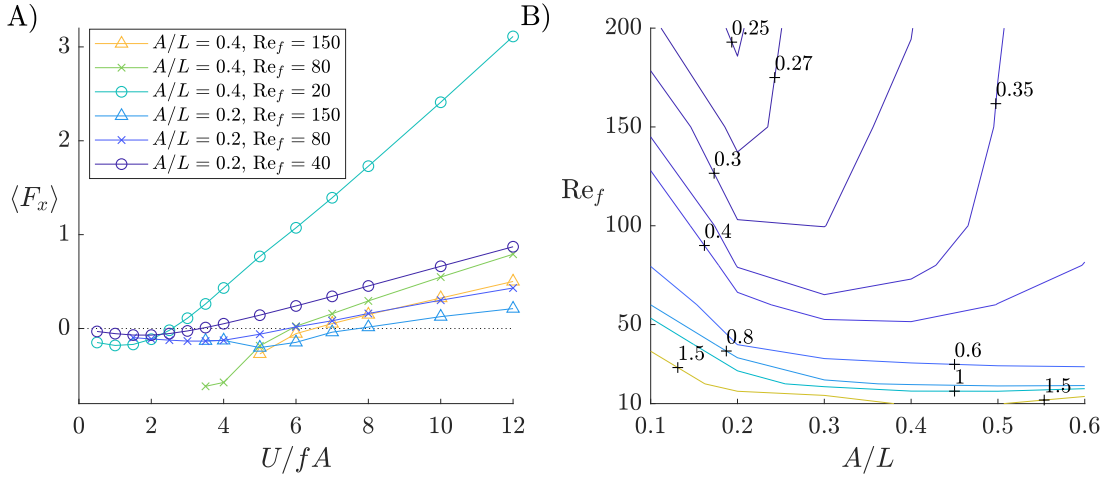


FIG. 6: A) Average horizontal force $\langle F_x \rangle$ versus normalized flow speed $U/fA = 2/St$. B) Contour map of Strouhal numbers corresponding to the self-propelled state ($\langle F_x \rangle = 0$) of a single flapping plate, in the space of dimensionless frequency (Re_f) and amplitude (A/L).

extending from zero; this interval becomes larger as Re_f increases. The curves at the lowest Re_f have a U-shape to the right of zero velocity, indicating that zero velocity is an unstable equilibrium and the self-propelled state is the single stable equilibrium.

To quantify the general features of the self-propelled state, and at smaller oncoming flow speeds, the efficiency-maximizing state, we compute $\langle F_x \rangle$ and η_{Fr} across a wide range of dimensionless frequencies (Re_f) and amplitudes (A/L). Figure 6B shows St_{SPS} , the Strouhal numbers of the self-propelled states, where $\langle F_x \rangle = 0$. The numbers grow rapidly as Re_f decreases to zero, and we expect divergence at a certain Re_f , as there is apparently no self-propelled state below a critical Re_f in experiments with rectangular plates [24] and simulations of thin ellipses [25]. For a given Re_f , the Strouhal number is fairly uniform as A/L varies, indicating that, like steady flows past cylinders [127] the self-propelled state corresponds approximately to a certain vortex street aspect ratio (roughly St) that is only slightly modified by A/L . Also, St_{SPS} varies smoothly in this region of parameter space, reflecting fairly uniform properties of the reverse von Kármán street and higher vortex street modes (i.e. the purple box in the top row of figure 5).

We have seen the maximum Froude efficiency state (approximately the green boxes in figures 4 and 5) occurs at a somewhat lower speed (higher St) than the self-propelled state (purple boxes). In figure 7A we plot contours of maximum-efficiency St and find a pattern of the contours is very similar to that in figure 6B, but with St roughly 50% higher in most of the plot. Panel B shows the values of the Froude efficiency maxima. Efficiency can only be positive above the critical Re_f at which self-propelled locomotion is possible. Not surprisingly, efficiency generally increases with Re_f , as vortex shedding becomes more significant. The efficiency reaches a maximum of 0.06 as Re_f increases to 200. Other experimental and computational studies have found the Froude efficiency is nearly unity at much higher Reynolds numbers [4, 128]. Panel B also shows that at small Re_f , the efficiency-maximizing $A/L > 0.6$, and gradually decreases to 0.2 as Re_f increases to 200.

The Froude efficiency is perhaps the most common measure of efficiency in flapping-foil studies, but it is not the only way to study optimal motions. One can also consider the state that maximizes a desired output (mean thrust,

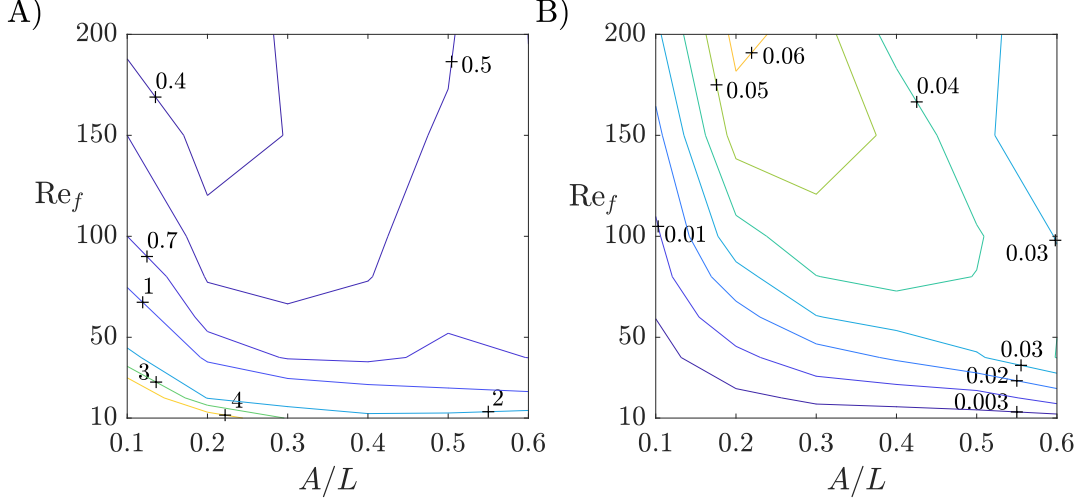


FIG. 7: A) Strouhal numbers corresponding to maximum Froude efficiency state of a single flapping plate, in the space of dimensionless frequency (Re_f) and amplitude (A/L). B) Values of Froude efficiency maxima.

or self-propelled speed, say) for various values of the input power [2, 129]. In figure 8 we map the two-dimensional space of flapping states with frequencies $Re_f \in [10, 200]$ and amplitudes $A/L \in [0.1, 0.6]$ to the space of self-propelled speed ($Re_{U,SPS} = LU_{SPS}/\nu$) (horizontal axis) and average input power $\langle \tilde{P}_{in} \rangle$ (vertical axis). The net of lines in the central portion of the figure is the image of a rectangle in $(Re_f, A/L)$ space; each solid line is a set of points with constant Re_f and each dashed line has constant A/L . The lines follow a common trend from lower left to upper right, showing that generally increased $Re_{U,SPS}$ correlates with increased $\langle \tilde{P}_{in} \rangle$. There is a smaller spread in the transverse direction. The Pareto frontier is the lower right boundary of the region: the set of points that maximize $Re_{U,SPS}$ for a given $\langle \tilde{P}_{in} \rangle$, or that minimize $\langle \tilde{P}_{in} \rangle$ for a given $Re_{U,SPS}$ [129]. This set provides an alternative definition of maximum efficiency, that provides different optima for a range of $\langle \tilde{P}_{in} \rangle$, and moving in the direction transverse to the Pareto frontier, we have increasing or decreasing optimality of states. One could also replace the desired output $Re_{U,SPS}$ with Froude efficiency, η_{Fr} , and allow U to vary as a third input. We discuss this alternative later in the paper. The vertical lines at the far right of the figure show the $(Re_f, A/L)$ values along the Pareto frontier for the ranges of $\langle \tilde{P}_{in} \rangle$ covered by these lines. The horizontal lines at the bottom show the $(Re_f, A/L)$ values along the Pareto frontier for the ranges of $Re_{U,SPS}$ covered by these lines. The vertical and horizontal lines show that the preferred flapping amplitude remains in the vicinity of 0.2-0.3 along the frontier, while the preferred frequency varies monotonically. In other words, to change speeds, it is most efficient to vary the frequency of the plate but keep its amplitude roughly fixed. A similar trend has been observed for the tail beats of various fish species as they vary their swimming speed [130].

For an isolated flapping body, the average horizontal force is sensitive to the oncoming flow speed (i.e. minus the swimming speed) as it increases from zero. The average force is zero (or close to zero) at zero oncoming flow speed, then becomes thrust, then decreases back to zero at the self-propelled state, then becomes drag as swimming speed

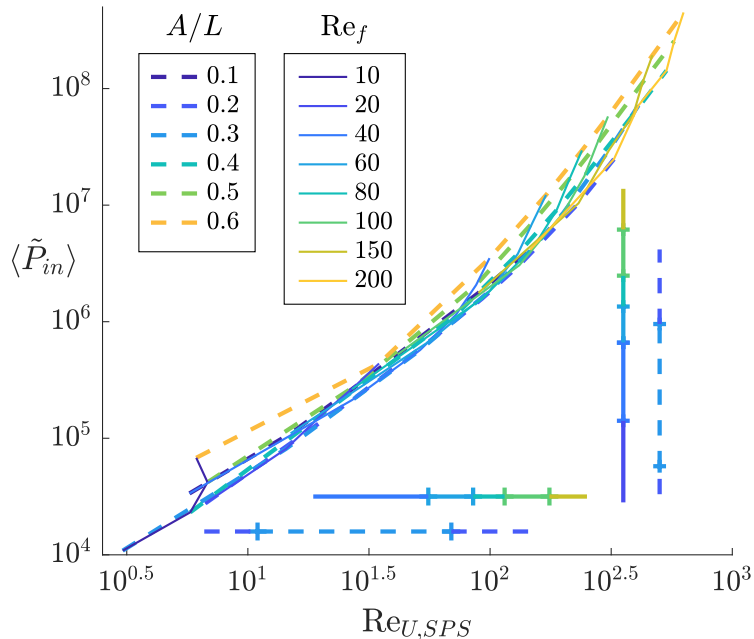


FIG. 8: Flapping states in the space of self-propelled speed ($Re_{U,SPS} = LU_{SPS}/\nu$) (horizontal axis) and average input power $\langle \tilde{P}_{in} \rangle$ (vertical axis). Solid lines denote states with a given flapping frequency (Re_f) and dashed lines are states with a given flapping amplitude A/L .

increases. These changes reflect changes in the vortex wake structure in the vicinity of the reverse von Kármán street, and the horizontal force has a subtle dependence on Re_f , A/L , and St . The input power, by contrast, has a simpler dependence on the parameters, as shown in figure 9. Panel A shows that $\langle P_{in} \rangle / Re_f^3$ is roughly constant with respect to St , with Re_f varying over a factor of 20 (values listed at bottom right), but depends strongly on A/L (values at right). The dependence on A/L is approximately scaled out by dividing by $(A/L)^3$, as shown by the collapse of lines in panel B, particularly at larger Re_f . Since the vertical plate velocity scales as $(A/L)Re_f$, $\langle \tilde{P}_{in} \rangle$ scales as vertical velocity cubed, a typical high-Reynolds-number scaling for a bluff body. Unlike the horizontal force, $\langle \tilde{P}_{in} \rangle$ is relatively insensitive to the oncoming flow speed (i.e. St) and the changes in vortex wake patterns shown in figures 4 and 5.

V. DOUBLY PERIODIC LATTICES OF PLATES

Having established some of the main properties of an isolated flapping plate in an oncoming flow, we now discuss the much larger space of doubly periodic lattices of flapping plates. We consider two types of lattices, rectangular and rhombic (diamond), shown in figure 1, also considered by [78, 80, 84, 86, 91]. Between these two lattices is the full range of 2D (oblique) lattices. We focus only on the two endpoint lattice types (rectangular and rhombic) because the remaining parameter space is already quite large (five-dimensional). For the rectangular lattice, we solve the flow in a single unit cell (figure 1A, dashed line box) with periodic boundary conditions. For the rhombic case, we solve the flow in a domain consisting of two unit cells (figure 1B, dashed line box), to observe when flow modes arise that

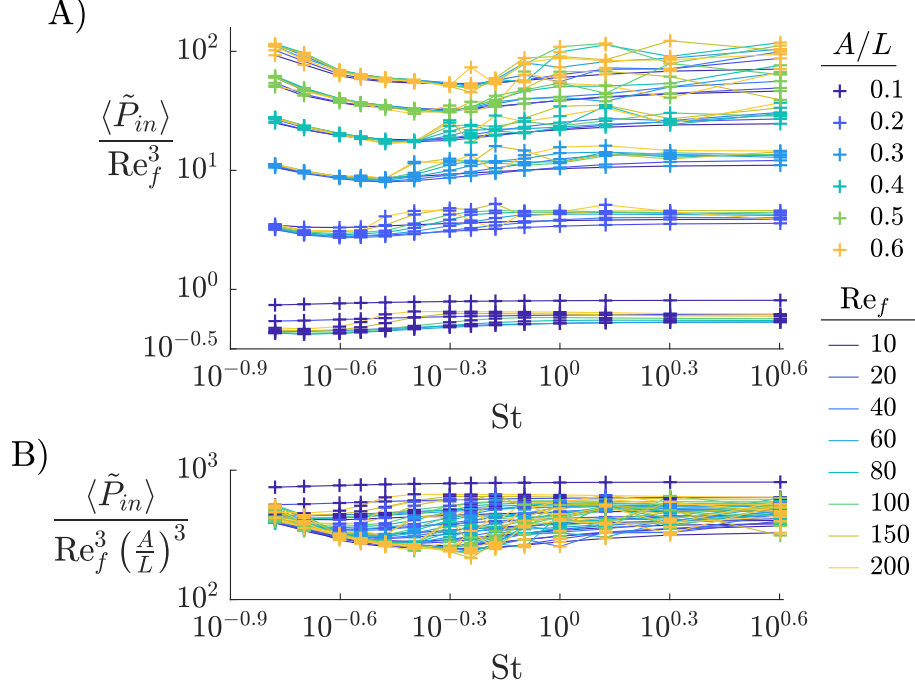


FIG. 9: For an isolated flapping body, the dependence of average input power $\langle \tilde{P}_{in} \rangle$ on frequency Re_f , amplitude A/L , and swimming speed St .

are periodic on length scales longer than a single unit cell. We focus on time-periodic dynamics for the most part, because such states are generally reached within 5-30 flapping periods. Dynamics usually appear to be nonperiodic at larger Re values, and may therefore require much longer run times to compute long-time averages with high accuracy. We generally avoid presenting time-averaged values for these cases except where noted explicitly in the text (e.g. for the average input power).

Figure 10A–D shows the average horizontal force $\langle F_x(t) \rangle$ versus normalized horizontal flow speed $U/fA = 2/\text{St}$ for a rectangular lattice of plates at $\text{Re} = 20$ and various l_x and l_y values. In the single-body case, the sidewall and upstream boundary conditions may cause numerical instabilities when vortices collide with these boundaries, i.e. when the oncoming flow speed is too small to advect vortices to the downstream boundary. This issue does not arise with doubly-periodic boundary conditions, and the flow computations remain stable with small oncoming flow speeds, so unlike in figure 6A, in 10A–D the curves can be computed down to zero U/fA . Panel A shows four curves with $A/L = 0.2$, $l_y = 1$, and l_x ranging from 1.2 to 1.5 (labeled at right). The vertical gap is one plate length, but the horizontal gap is smaller, 0.2 to 0.5. $\langle F_x \rangle$ initially increases with U/fA , so unlike a single flapping plate at this Re , zero velocity is a stable equilibrium here. After reaching a peak, each curve drops (sharply for $l_x = 1.2$, then more smoothly as l_x increases), and then adopts a U-shape somewhat similar to that in the isolated body case. For $l_x = 1.2$ to 1.4, there are three zero crossings (counting $U/fA = 0$), corresponding to three equilibria, two stable and one unstable. Panel B shows the same data with l_y increased to 1.5. The darkest blue curve ($l_x = 1.2$) now has two

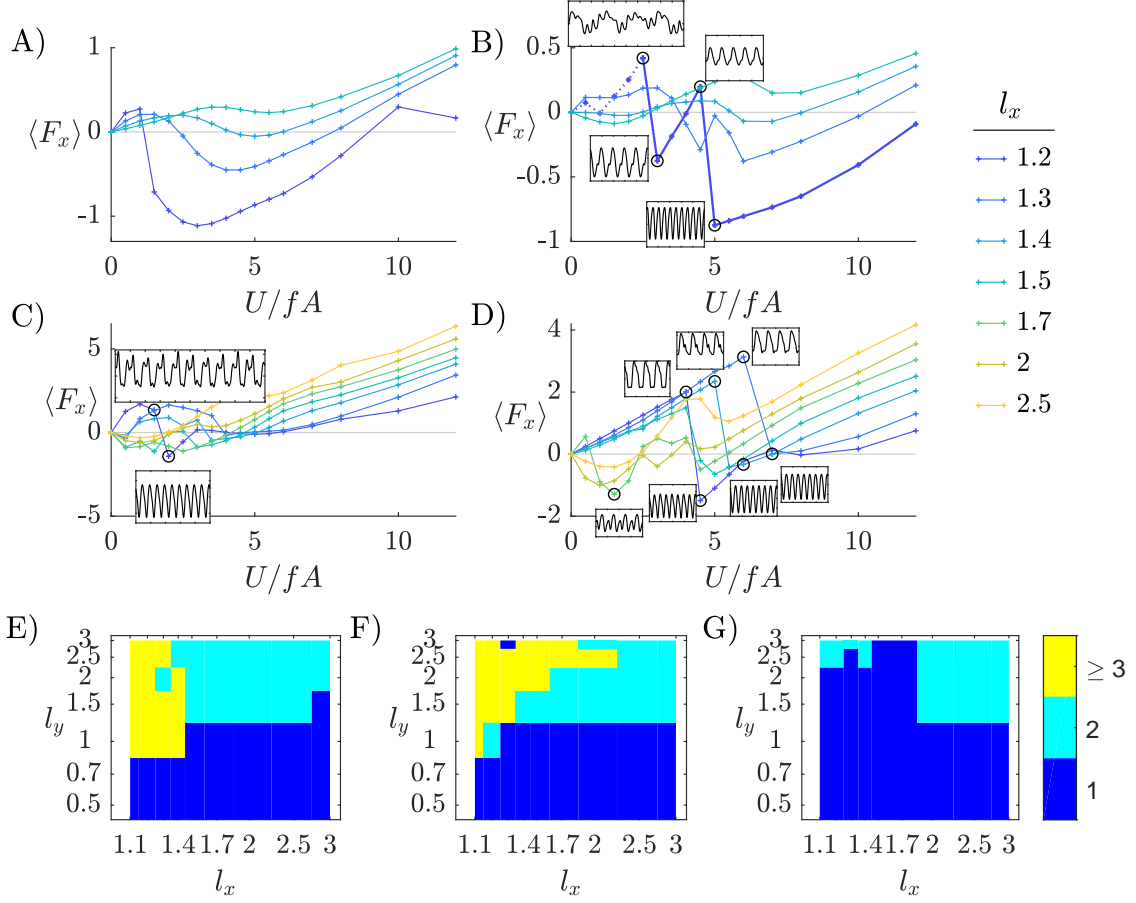


FIG. 10: Average horizontal force $\langle F_x(t) \rangle$ versus normalized horizontal flow speed $U/fA = 2/St$ for $Re = 20$ and various l_x and l_y values. In panels A-D, each line plots $\langle F_x(t) \rangle$ versus U/fA for various l_x , listed at right. Specific values of A/L and l_y are chosen for each of the panels A-D: A) $A/L = 0.2$, $l_y = 1$, B) $A/L = 0.2$, $l_y = 1.5$, C) $A/L = 0.5$, $l_y = 2$, D) $A/L = 0.5$, $l_y = 3$. Bottom row: for various (l_x, l_y) pairs, the number of equilibrium states (U/fA with $\langle F_x(t) \rangle = 0$), for $A/L = 0.2$ (E), 0.5 (F), and 0.8 (G).

sharp drops, between which the curve increases with U/fA . Near zero U/fA , the curve is dotted, indicating that the dynamics are nonperiodic in this region, so in the averages on the dotted line there is some uncertainty (that we do not quantify here). At the last of these nonperiodic cases (highest circled point), the time trace of $F_x(t)$ is shown in a small inset panel, with tick marks every flapping period along the horizontal axis. The graph of $\langle F_x(t) \rangle$ then drops sharply to the next point, also circled, at which the time trace becomes periodic with period 1. The dynamics remain 1-periodic as $\langle F_x(t) \rangle$ increases to the next circled point. Then $\langle F_x(t) \rangle$ drops sharply again, to a state that is 1/2-periodic, the fourth and final circled point on this curve. The curve then increases smoothly with further increases in U/fA . In this case, the sharp drops in the curve correspond to changes in periodicity, from nonperiodic, to 1-periodic, to 1/2-periodic. We will discuss the corresponding flow structures below. The remaining curves in this panel, for $l_x = 1.3$ to 1.5 , become increasingly smooth as l_x increases, eventually resembling those in panel A, but with an additional equilibrium for $l_x = 1.4$ and 1.5 ; zero velocity is unstable for these cases. Panel C shows the

same quantities for A/L increased to 0.5 and l_y increased to 2, and a wider range of l_x (labeled at right). The two inset panels show another example of the change in dynamics (from 4-periodic to 1/2-periodic) that accompany a sharp drop in $\langle F_x \rangle$ at a particular U/fA . Panel D ($l_y = 3$) shows three more examples of changes from 1-periodic to 1/2-periodic dynamics that occur at sharp drops in $\langle F_x \rangle$. Panels C and D indicate a transition with respect to l_x as well. For l_x near 1 (blue curves), the plates experience drag at small U/fA . At larger l_x (green and yellow curves), more complex variation of $\langle F_x \rangle$ is seen at small U/fA including thrust. By counting the numbers of zero crossings of these curves (including $U/fA = 0$), we obtain the number of equilibrium states, and show the totals as colored patches in the bottom row, for $A/L = 0.2$ (E), 0.5 (F) and 0.8 (G). In the dark blue regions $U/fA = 0$ is the only equilibrium, and there is no net locomotion. This is the case at smaller l_y in most cases, and some larger l_y values at the largest A/L (panel G). The close vertical stacking of adjacent bodies tends to suppress vortex formation and thrust generation, as we will illustrate later. In the light blue regions, there are two equilibria: $U/fA = 0$ is unstable and there is a stable self-propelled state, as in the isolated-body case. Examples are given by the yellow lines in panels C and D, which represent the closest approximation to the isolated body among these cases (l_x and l_y are largest). However, the body might not be well approximated as isolated in some cases; there can be significant flow interactions across the periodic unit cell, particularly at $A/L = 0.5$ and 0.8. The yellow regions in the bottom row of panels have three or more equilibria, and these generally correspond to small l_x and large l_y . The interactions between adjacent bodies' edges are strongest here, and lead to a variety of flow modes (and dynamics, indicated by the insets we have discussed) that are sensitive to small changes in U/fA and the other parameters. At the largest A/L (panel G), these states are suppressed by the larger amplitude of motion, which tends to suppress interactions between vortices shed by horizontally adjacent plates.

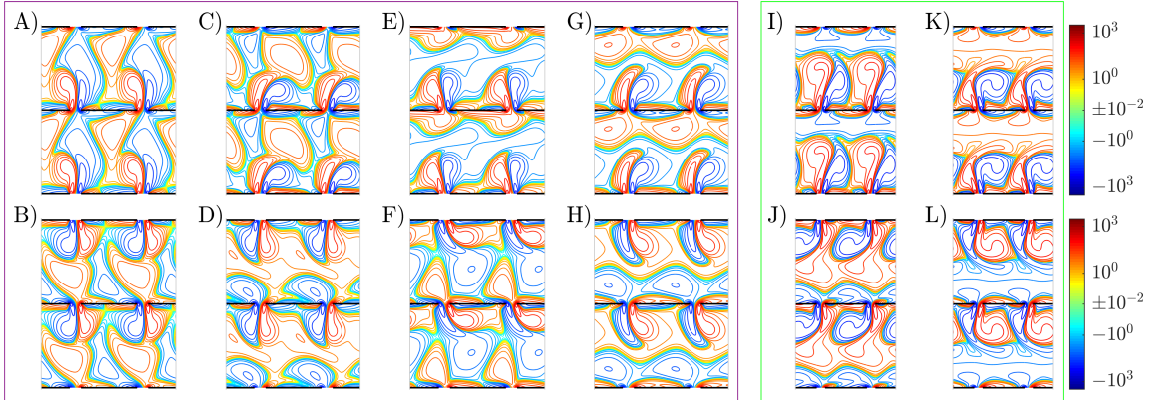


FIG. 11: Flow states that accompany the sudden drops in $\langle F_x \rangle$ highlighted in figure 10B (purple box) and C (green box). Panels A-B and C-D show vorticity snapshots 1/2-period apart, before and after the first sudden drop in $\langle F_x \rangle$ shown by circles in figure 10B. Panels E-F and G-H correspond to the second drop in figure 10B. The green box shows the flow state transition for the drop in figure 10C.

Figure 11 shows examples of the flows near the sudden drops in $\langle F_x \rangle$. In figure 10B, four circled data points are shown, bracketing two sudden drops in $\langle F_x \rangle$. Corresponding flows, at two instants spaced 1/2 of a flapping period apart, are shown by the four pairs of panels in the purple box of figure 11. Panels A-B show the flow at U/fA slightly below the first circled data point, in a quasi-periodic state giving drag. In panel A, the upward flow through

the thin gap between adjacent plate edges produces an asymmetric vortex dipole. In panel B, a $1/2$ -period later, the downward flow produces a similar asymmetric dipole. In both cases, although the net flow is rightward, the vortices on the leftward sides of the dipoles are larger. Panels C and D show the corresponding flows at the second circled point in figure 10B, after the first sudden drop in $\langle F_x \rangle$, to a state of net thrust. Again, two vortex dipoles are produced on each half-cycle, but now the upward dipole curves rightward (downstream), and the rightward (blue) vortex is larger. However, the downward dipole is still roughly symmetric. Panels E and F show the corresponding flows at the third circled point in figure 10B. The downstream flow is larger, and net drag is obtained. In panel E, the upward dipole is more symmetric, similar to the downward dipole in panel D, and the downward dipole in panel F is curved downstream, like that in panel C. Panel G and H show the flows at the fourth circled point in figure 10B, after the second sudden transition from a state of drag to a state of thrust. Now both dipoles are curved rightward. Panels G and H also show a flow state that is up-down symmetric after a $1/2$ -period. Consequently, $F_x(t)$ (inset next to fourth circle in figure 10B) is $1/2$ -periodic—the horizontal force is the same on the up and down strokes. By contrast, the first, second, and third flow states were not up-down symmetric, and $F_x(t)$ was 1-periodic in each case. A similar phenomenon occurs at the sudden drop in $\langle F_x \rangle$ accompanied by the insets in figure 10C. $F_x(t)$ transitions from 4-periodic to $1/2$ -periodic in the insets. Flow snapshots are shown in the green box of figure 11; panels I-J for the first inset of figure 10C, and panels K-L for the second. In panels I-J, the vortex dipoles are not up-down symmetric after a $1/2$ -period, and the upstream member of each vortex pair is larger. In panels K-L, the dipoles are up-down symmetric, and the downstream vortices are larger. A similar phenomenon also occurs at each of the three sudden drops in $\langle F_x \rangle$ highlighted by circles in figure 10D. The corresponding flow transitions, from up-down asymmetric to symmetric, are shown in figure 30 in appendix A. The general phenomenon then is that sudden changes from drag to thrust can occur when l_x is close to 1, when the dipole jets on each half stroke switch from upstream to downstream orientations. As l_x increases to larger values, the curves may become smoothed versions of those with sharp drops, e.g. in figure 10A. Eventually, at large enough l_x , the vortex shedding pattern changes qualitatively from a dipole between adjacent leading and trailing edges, to a single dominant vortex that interacts with previously shed vortices in the wake, e.g. the reverse von Kármán street.

Figures 10, 11, and 30 have shown that for l_x near 1, $F_x(t)$ can sharply change from 1-periodic (or 4-periodic) to $1/2$ -periodic at certain oncoming flow speeds. Figure 12 shows further examples of the diversity of periodic $F_x(t)$ that can occur when l_x is near 1. Panels A and B show $1/2$ -periodic $F_x(t)$, the first roughly sinusoidal, the second far from it. Panel C shows a 1-periodic state. Panels D and E show 1.5-periodic states, with repeated features highlighted in red. Panel E can be regarded as a perturbation of a $1/2$ -periodic state. Panels F and G are 2-periodic states with repeated features highlighted in green; panel F is nearly $1/2$ -periodic, while panel G is nearly 1-periodic. Panel H shows that the dynamics can switch between different nearly-periodic states over long periods of time. The blue regions last for 2.5 periods, while the red-regions are nearly 3-periodic, and their recurrences (with slight changes) do not follow a simple pattern up to $t = 30$. Panel I shows the 4-periodic state of figure 10C, top inset, with repeated features highlighted in orange; the state is nearly 1-periodic. Panel J shows a nonperiodic state that nonetheless has recurrent downward spikes near certain times that are spaced by multiples of 0.5: $t = 3.2, 5.7, 7.2, 8.2, 10.2, \text{ and } 11.7$.

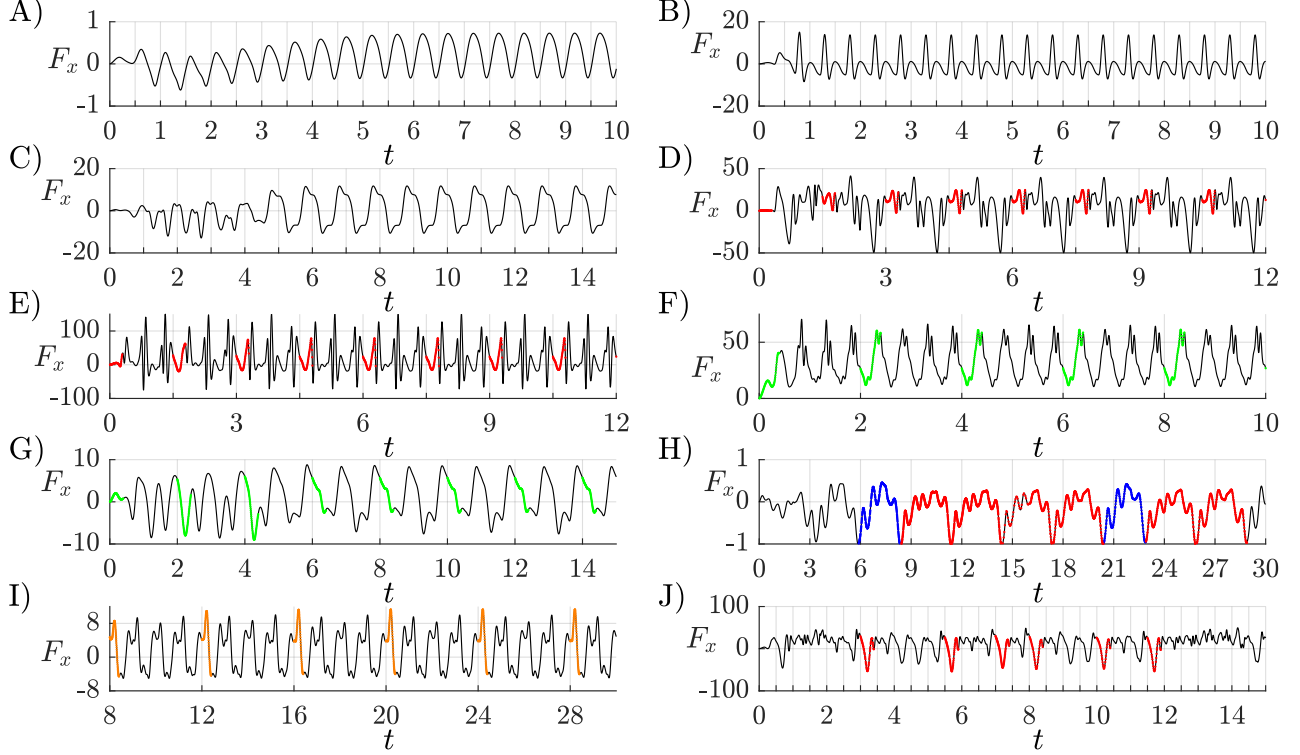


FIG. 12: Examples of $F_x(t)$ exhibiting various types of periodicity when l_x is close to unity. All occur for rectangular lattices with $\text{Re} = 20$. A) $A/L = 0.2$, $l_x = 1.2$, $l_y = 1$, $U/fA = 1$; B) $A/L = 0.5$, $l_x = 1.2$, $l_y = 1$, $U/fA = 1$; C) $A/L = 0.5$, $l_x = 1.2$, $l_y = 3$, $U/fA = 1$; D) $A/L = 0.8$, $l_x = 1.1$, $l_y = 2$, $U/fA = 0.5$; E) $A/L = 0.8$, $l_x = 1.1$, $l_y = 1$, $U/fA = 4.5$; F) $A/L = 0.8$, $l_x = 1.2$, $l_y = 1$, $U/fA = 12$; G) $A/L = 0.5$, $l_x = 1.3$, $l_y = 2$, $U/fA = 3.5$; H) $A/L = 0.2$, $l_x = 1.2$, $l_y = 2$, $U/fA = 1$; I) $A/L = 0.5$, $l_x = 1.2$, $l_y = 2$, $U/fA = 1$; J) $A/L = 0.8$, $l_x = 1.1$, $l_y = 2$, $U/fA = 10$.

Figure 13 shows examples of flows for which $F_x(t)$ has a period larger than unity. Panels A-D show snapshots, a $1/2$ -period apart, that correspond to figure 12D. Panel A shows an upward dipole, followed in panel B by a downward dipole. Panel C shows a smaller upward dipole, and then panel D is a mirror image of panel A. The next two snapshots (not shown) would be mirror images of panels B and C, followed by a return to panel A. Thus $F_x(t)$ has period 1.5 and the flow has period 3. Panels E-I show a flow with period 2, and with $F_x(t)$ of period 2. The upward, rightward curving dipole in panel A is followed by a straighter downward dipole in panel F. The dipole in panel G is more curved than panel E, while that in panel H is similar to that in panel F. With panel I, the flow returns to panel E. This flow is a more slightly perturbed version of a 1-periodic flow than the flow in panels A-D, as are many of the n -periodic flows we have observed.

We have studied examples of $F_x(t)$ and flows with different periods, mainly for l_x close to 1. More broadly, there is a gradual trend towards nonperiodicity at certain parameter values. For $\text{Re} = 20$, and three different A/L (0.2 (A), 0.5 (B), and 0.8 (C)), we plot circles in figure 14 where $F_x(t)$ deviates from 1-periodicity by the following measure. We compute the averages of $F(t)$ over the last eight half-periods of $V(t)$, during $t = 11$ to 15. We split the eight values into two sets of four, one for the first half-period of $V(t)$ and the other for the second half-period. We sum the standard

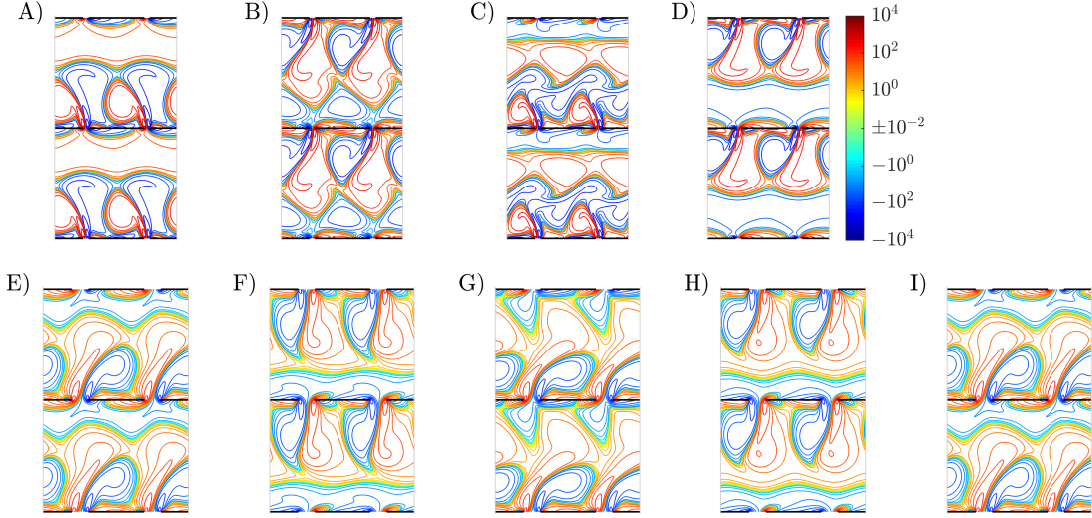


FIG. 13: Flows exhibiting different periodicities. Panels A-D: Snapshots spaced by 0.5 corresponding to $F_x(t)$ in figure 12D. Panel D is essentially a mirror image of panel A. Panels E-I: Snapshots spaced by 0.5 for a 2-periodic flow ($\text{Re} = 20$, $A/L = 0.5$, $l_x = 1.3$, $l_y = 2$, and $U/fA = 3$).

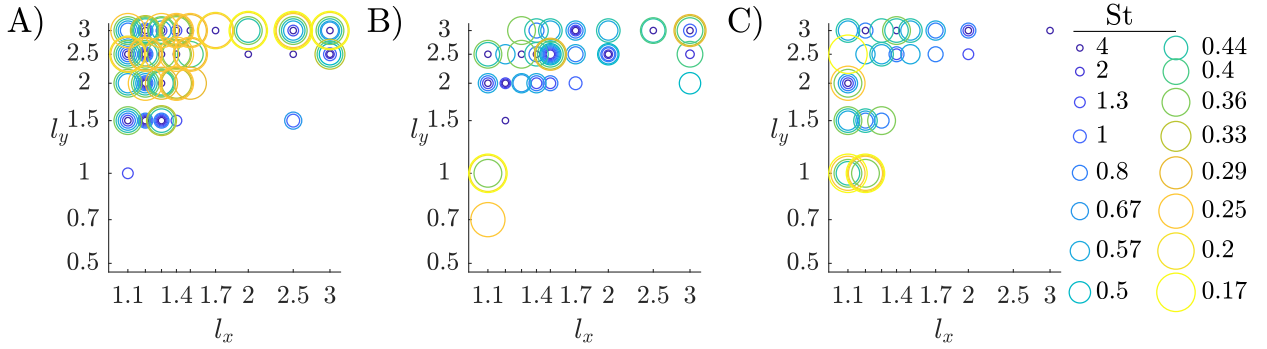


FIG. 14: Circles show parameter values where $F_x(t)$ falls below a threshold 0.01 (described in text) for having period 1, for a rectangular lattice of plates with $\text{Re} = 20$. Values of A/L are 0.2 (A), 0.5 (B), and 0.8 (C). Values of St (note $U/fA = 2/\text{St}$) are labeled by circle size and color (key listed at right). Circles are centered at the corresponding values of l_x and l_y .

deviations over the two sets and normalize by $\frac{1}{4} \int_{11}^{15} |F_x(t)| dt$ (an average magnitude of F_x). Where the resulting value is greater than 0.01, we plot circles in figure 14. The 0.01 threshold is somewhat arbitrary, but is chosen with certain considerations in mind. The flapping motion imposes a strong 1-periodic component in all flows, so a threshold of 0.1, say, would classify some nonperiodic $F_x(t)$ as periodic. A threshold much smaller than 0.01 would miss some $F_x(t)$ that have almost but not completely converged to periodic near $t = 15$. The circles occur predominantly at large l_y , and more often at small l_x , though they are also found at large l_x . The reason is that the close spacing of plates at small l_y tends to suppress complex vortical structures, and leads to more laminar, periodic flows. As we have seen, small l_x leads to formation of thin dipole jets with sharp concentration of vorticity, and complicated nonperiodic dynamics can result. Many of these cases occur at small oncoming velocity (large St), reflected in the larger number

of small blue circles across the panels. As we have seen for the isolated body, above a certain flow speed, a reverse von Kármán street tends to form, in many cases due to merging or other regular interactions between the leading and trailing edge vortices. The larger number of yellow circles at $A/L = 0.2$ (panel A) is perhaps because at a given U/fA , U/fL is smaller in panel A, so in a given flapping period, vortices do not move as far downstream relative to the plate length in this case, leading to more complicated dynamics. Also, Re is constant (20) in all three panels, so Re_f decreases from left to right. To the extent that viscous regularizing effects are more controlled by Re_f , they are increased moving from left to right. The corresponding data for the rhombic lattice are shown in figure 31 in the appendix, and shows similar trends but with additional nonperiodic states at smaller l_y .

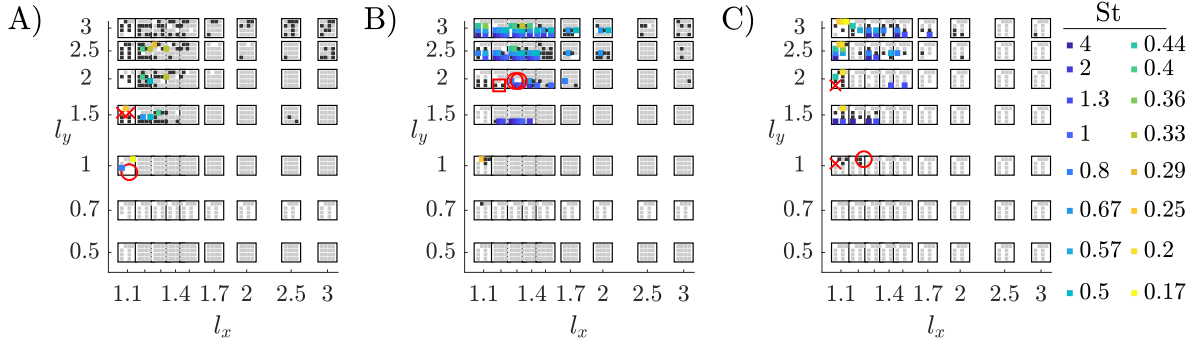


FIG. 15: Flows at $Re = 20$ for a rectangular lattice, classified by type of periodicity, with $A/L = 0.2$ (A), 0.5 (B), and 0.8 (C). Each box shows data for a certain (l_x, l_y) pair that is located at the box center, and contains a set of smaller squares, each for a different value of St ranging from 0.17 to 4 (listed at right, note $U/fA = 2/St$). The gray boxes correspond to $F_x(t)$ with period 0.5. The colored boxes correspond to period 1 but not period 0.5, i.e. flows that are not up-down symmetric. For these flows only, we use the colors to label the St value. The black boxes denote nonperiodic $F_x(t)$.

Figure 15 shows information about the types of periodic states that occur in parameter space, some corresponding to the $F_x(t)$ and flows shown in figures 10-13. The panels again show states at $A/L = 0.2$ (A), 0.5 (B), and 0.8 (C). Within each panel are a set of boxes (black outlines), each centered at the corresponding (l_x, l_y) pair. Each box contains a set of smaller squares, each for a different value of St ranging from 0.17 to 4 (listed at right, note $U/fA = 2/St$). The gray squares correspond to $F_x(t)$ with period 0.5. The colored squares correspond to period 1 but not period 0.5, i.e. flows that are not up-down symmetric. For these flows only, we use the colors to label the St value. The black squares are for nonperiodic $F_x(t)$, the cases shown by circles in figure 14. White spaces lie within some of the boxes because not all parameter combinations were computed, but the overall pattern is not altered by these omissions. At $Re = 20$, most squares are gray, so most flows are up-down symmetric. The colored squares (1-periodic states) occur mainly at smaller l_x and larger l_y . They are most prevalent at the intermediate A/L (panel B), and there they occur at large St , i.e. smaller U/fA . We have also noted a few cases of $F_x(t)$ with longer periods: 1.5 (red crosses), 2 (red circles), and 4 (red square), all of which occur at small l_x . In general, the period-1 and longer-period states occur near the nonperiodic states (black squares), so the former may be intermediaries in the transition from 1/2-periodic to nonperiodic states as the parameters are varied to allow more disordered flows.

Figure 16 shows the same quantities when the lattice is changed from rectangular to rhombic. The general trend

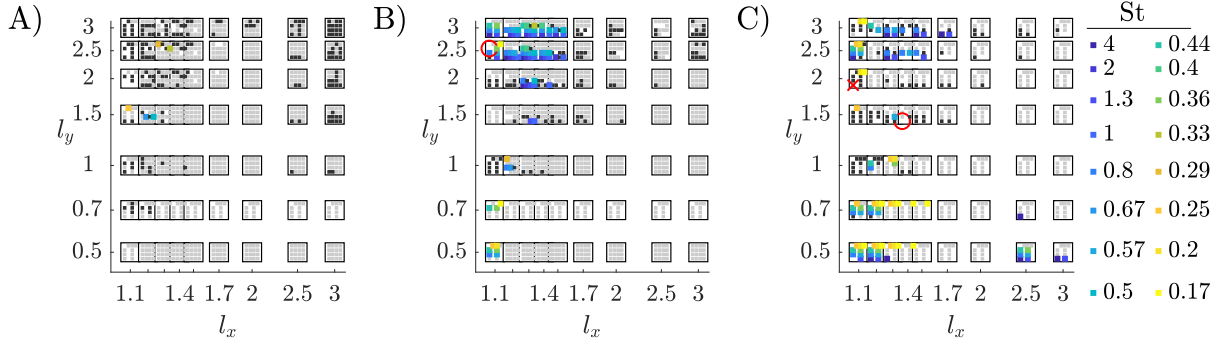


FIG. 16: Flows at $\text{Re} = 20$ for a rhombic lattice, classified by type of periodicity, with $A/L = 0.2$ (A), 0.5 (B), and 0.8 (C). Each box shows data for a certain (l_x, l_y) pair (at the box center), and contains a set of smaller squares, each for a different value of St ranging from 0.17 to 4 (listed at right, note $U/fA = 2/\text{St}$). The gray boxes correspond to $F_x(t)$ with period 0.5 . The colored boxes correspond to periodicity unity but not periodicity 0.5 , i.e. flows that are not up-down symmetric. For these flows only, we use the colors to label the St value. The black boxes denote nonperiodic $F_x(t)$.

of $F_x(t)$ with increasing period or non-periodic at smaller l_x and larger l_y is basically preserved. Compared to the rectangular lattice data, there are more 1-periodic and nonperiodic $F_x(t)$ at small l_y . This is perhaps because there is more y -distance between adjacent bodies for the rhombic lattice than for a rectangular lattice at the same l_y , allowing for more complex flows.

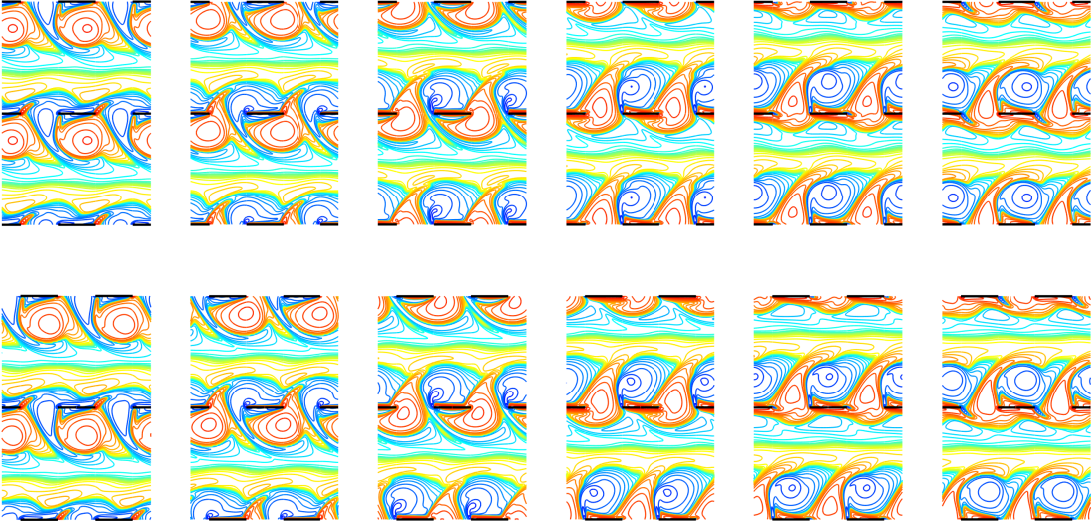


FIG. 17: Six vorticity snapshots spaced by 0.1 in t during the half-period of upward flow, for rectangular (top row) and rhombic (bottom) lattices. The parameters are $A/L = 0.5$, $l_x = 2$, $l_y = 3$, $\text{Re} = 70$, and $U/fA = 7$.

One important limiting case is the large- l_y limit. Here the configuration consists of well-separated 1D arrays of flapping plates. The flows around the 1D arrays are essentially the same for the rectangular and rhombic lattices.

Figure 17 presents an example of such a flow, at $l_x = 2$ and $l_y = 3$. The top row is a sequence of vorticity snapshots during the half-period of upward flow relative to the plates, for a rectangular lattice. The six snapshots are spaced apart by 0.1 in t . The positive (orange) vortices below the plates in the first panel, shed from the leading edge on the previous half-period, now merge with positive vorticity shed from the trailing edge during this half period. This is a case of relatively high Froude efficiency. The main difference from an isolated plate is the close interaction between the vortices shed at the leading and trailing edges of adjacent bodies, and the blue vortices are above the orange vortices, the opposite of the reverse von Kármán streets of figures 4 and 5, and more similar to a regular von Kármán street (albeit with plates among the vortices). The lower row shows the same flow for a rhombic lattice of plates. The flow is almost the same, because there is little interaction between vertically adjacent rows. A double layer of weak vorticity (light blue, green, and yellow) separates the vortex arrays of each row. In this region, the flow velocity is approximately uniform, with vertical flow speed equal to the average vertical flow speed, and horizontal flow speed about twice the average horizontal flow speed. The horizontal flow speed in the plate/vortex array is both positive and negative, and much smaller in magnitude.

We now show examples of how the large- l_y flows change as l_x and A/L are varied, in figure 18. We choose $Re = 20$ and $U/fA = 3$ (large enough that regular vortex arrays may be generated, and small enough that thrust may occur). In the top row, $A/L = 0.2$. Moving left to right, as the gap between adjacent plates increases, the flow changes from a dipole to a vortex street. At far right, the trailing edge vortices interact more with the previously shed trailing edge vortex than with that shed at the leading edge of the adjacent plate. There is mean thrust for the flows in the first two columns of the top row, approximately zero thrust for the third, and small net drag for the fourth. In the second row, $A/L = 0.5$, there is again a transition from dipole jets to a vortex street, with larger vortices now. Now there is also nontrivial coupling between adjacent rows of plates. Instead of uniform flow, in the first three panels there are bands of nearly constant vorticity above and below the vortex arrays. These are shear flows with u nearly linear with respect to y and v nearly constant. They differ from those that would be seen with an isolated flapping body, and therefore, unlike the flows in the first row, they would be altered for larger l_y values. In the second row, only the third column corresponds to a state of mean thrust. In the third row, $A/L = 0.8$, only the first column is a state of mean thrust. It is not obvious from the form of the vortex dipole why mean thrust occurs, but there are noticeable differences with the orientation of the dipole in the second panel. Again there are linear shear zones above and below the dipole jets. In the fourth column, vertical bands of same-signed vorticity form. Now the plates are coupled strongly to both vertical and horizontal neighbors through the flow.

We have shown examples of flows with l_y fixed and l_x from small to large. We now reverse the parameters, i.e. hold l_x fixed at 2 (an intermediate value), and vary l_y from small to large. Figure 19 shows examples of vorticity fields at instants of upward (and as usual, rightward) flow. Since l_y may be small, there can be significant differences between rectangular and rhombic lattice flows and we show both. The differences are most pronounced at the smallest l_y . In panels A and C ($l_y = 0.2$ and $U/fA = 3$ and 7, respectively), the flow through the rectangular lattice is approximately horizontal Poiseuille flow between the vertical neighbors (away from the plate end regions), and unidirectional vertical flow in the space between horizontal neighbors. Most of the vertical flux occurs in these vertical channels, and the flow

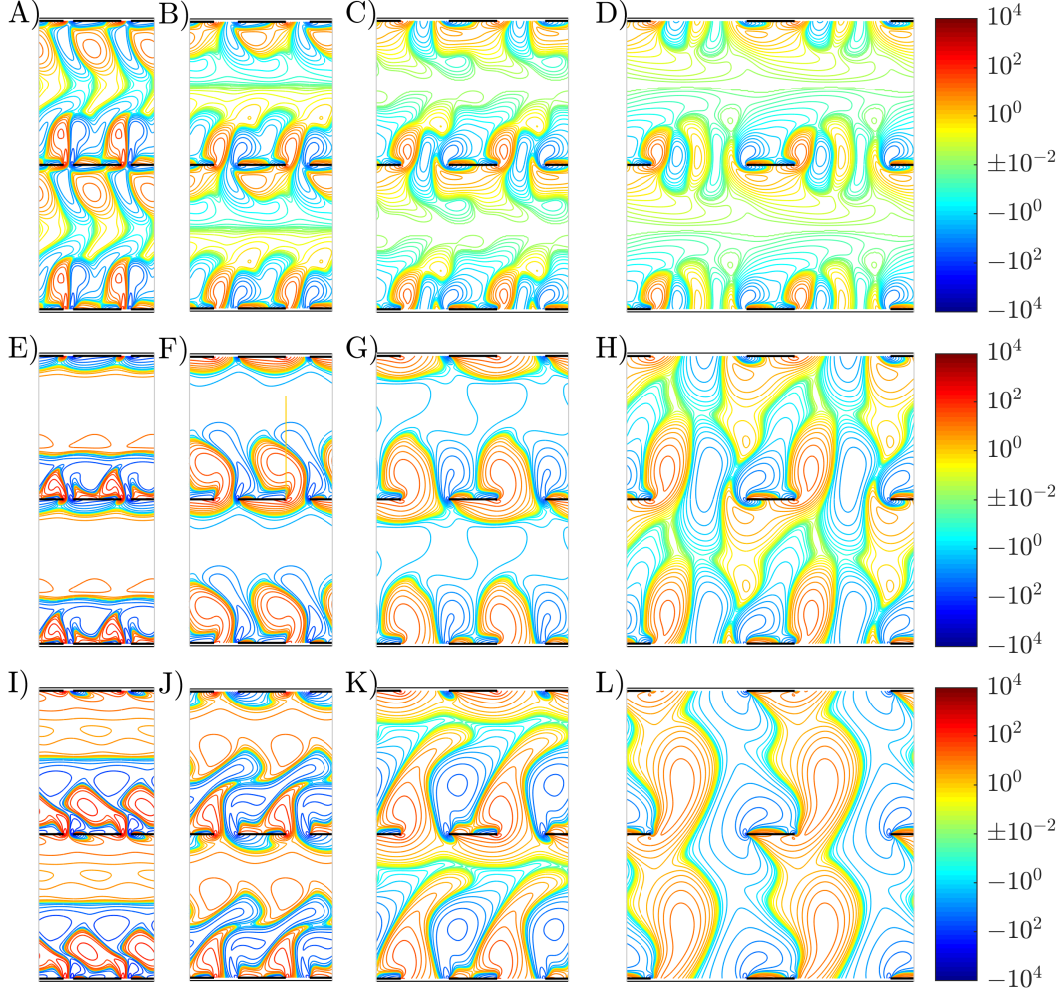


FIG. 18: Flow snapshots with $l_x = 1.2, 1.5, 2,$ and 3 (left to right columns) and $A/L = 0.2, 0.5,$ and 0.8 (top to bottom rows). The other parameters are: $Re = 20, U/fA = 3, l_y = 3$.

past the plate edges is relatively weak. These small- l_y flows result in a net drag force, almost constant in time, that of the Poiseuille flow between the plates. The corresponding rhombic lattice flows (B and D) are much more complex. The plates now cover the full horizontal extent of the flow field, so the entire flow is forced through the small gaps between the interleaving plate edges. Consequently, much stronger vorticity is generated at the plate edges. This flow results in a net thrust force, is not temporally periodic but $F_x(t)$ has a strong $1/2$ -periodic component, and is also not spatially periodic on the scale of a single unit cell (i.e. containing a single plate), but of course is periodic on the the scale of a double unit cell by the definition of the periodic boundaries (the dashed box in figure 1B). This can be seen by examining the flows below the right edges of the plates. There is a small blue vortex below the top plates' right edges, but a larger (B) or smaller (D) blue region below the middle plates' right edges. Increasing l_y to 0.5 , the rectangular lattice flows (E and G) deviate more from Poiseuille flow, while the rhombic lattice flows (F and H)

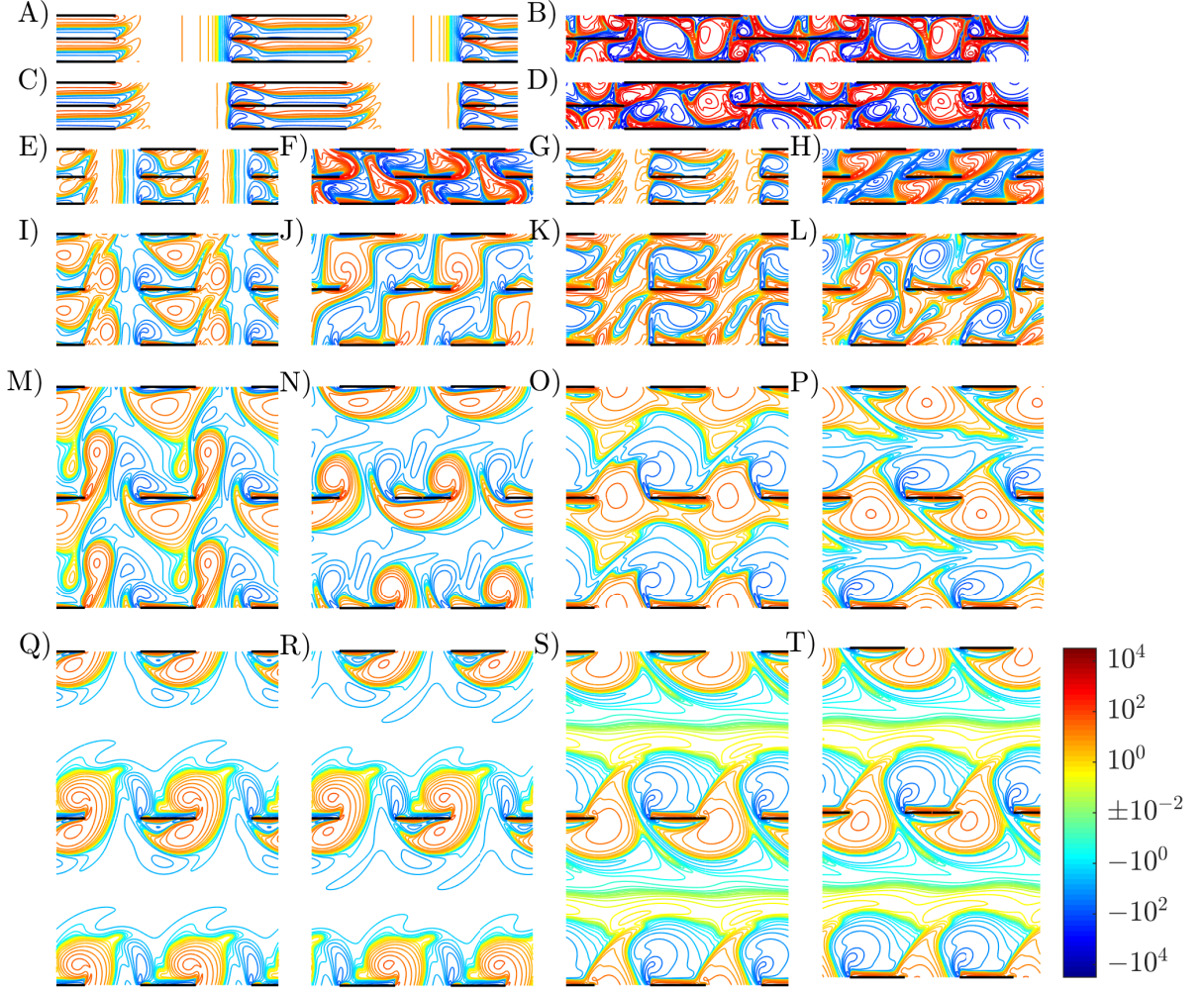


FIG. 19: Flow snapshots with $l_x = 2$ and various l_y : 0.2 (A-D), 0.5 (E-H), 1 (I-L), 2 (M-P), and 3 (Q-T). Within each group of four consecutive panels, the first two are for $U/fA = 3$ (A-B, E-F, I-J, etc.) and the second are for $U/fA = 7$. Within each of these two pairs of panels, the first is a rectangular lattice (A, C, E, G, etc.) and the second is a rhombic lattice. In all cases, $Re = 70$ and $A/L = 0.5$. The values of vorticity on the contours are labeled on the colorbar at lower right.

become smoother. Panel F, at lower U/fA , is still a temporally nonperiodic flow, but closer to spatially periodic on the scale of the unit cell than panels B or D. The flow in panel H is both temporally periodic and spatially periodic on the unit cell scale. Again, both rectangular lattice flows generate net drag, while the rhombic lattice flows generate net thrust. Increasing l_y to 1, both rectangular flows (I and K) again generate drag, though I, at lower U/fA , is close to zero net drag. Of the rhombic lattice flows (J and L), only J generates thrust, but with relatively high Froude efficiency (0.04), much higher than in panel F due both to increased thrust and decreased input power. Unlike the rectangular lattice, the rhombic lattice geometry allows an oblique vortex dipole to form at this l_y (panel J), involving a positive (orange) vortex at the right edges of the middle plates and a negative vortex (blue) at the left edges of the bottom plates, which probably underlies efficient thrust generation. Increasing l_y to 2, the rectangular lattice has the first occurrence of a state of net thrust in this figure, at low U/fA (M) but not high U/fA (O). The rhombic

lattice has a state of net thrust at both speeds (N and P). At the largest $l_y = 3$, the rectangular (Q, S) and rhombic (R, T) flows are similar as discussed below figure 17; both pairs generate net thrust with only small differences in their magnitudes and the corresponding Froude efficiencies. To summarize, for the rectangular lattice, only net drag occurs below a moderate l_y . For the rhombic lattice, by contrast, thrust can occur at very small l_y , though the flows are nonperiodic and the Froude efficiency is low. We can also see that the rhombic lattice flows converge to spatially periodic on the unit cell scale as l_y becomes large, which correlates with the convergence to temporal periodicity. By computing the relative error in unit-cell-periodicity for a number of other flows (76 in all) at various parameters, we find that unit-cell-periodicity correlates with temporal periodicity in general. Both are more prevalent when Re is small, and when $l_x - 1$ is not very small. However, there are examples of one without the other and vice versa. Therefore, in a large lattice of plates of plates at sufficiently large Re, the flow would be expected to deviate from the periodic lattice model with unit cell periodicity. However, in most cases considered in this paper, the deviation is not very large.

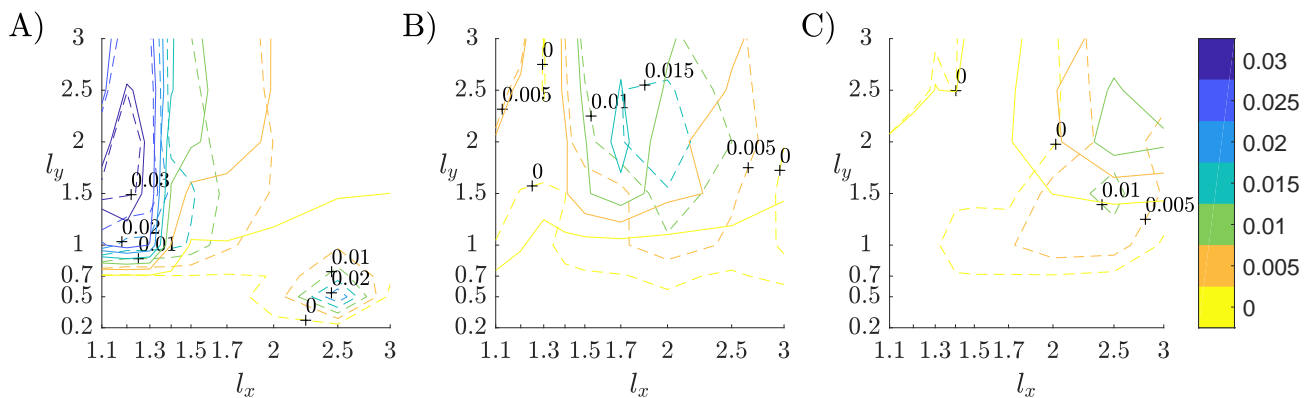


FIG. 20: Contours of Froude efficiency at $A/L = 0.2$ (A), 0.5 (B), and 0.8 (C), for rectangular (solid lines) and rhombic (dashed lines).

We have discussed some examples of plate-plate interactions that lead to thrust generation in certain one-dimensional slices through parameter space: at moderate and large l_y for different l_x (figures 11, 18, and 30), and for intermediate l_x at large l_y (figure 19). In the l_x - l_y plane, we present in figure 20 contour plots of Froude efficiency at smaller Re ($= 20$), where most flows are time-periodic. Contours are plotted for $A/L = 0.2$ (A), 0.5 (B), and 0.8 (C), for both rectangular (solid lines) and rhombic (dashed lines) lattices. In panel A, the dashed and solid lines are close for l_y above 2, with a very slight advantage for the rectangular lattice. At this A/L and large l_y , there is little interaction between different horizontal rows of plates, so the lattice type makes little difference, as in figure 17. Below $l_y = 2$, the solid contour lines bend sharply leftward, and efficient thrust is only obtained for l_x near 1, if at all. Here the rhombic lattice is more efficient, and yields net thrust down to $l_y = 0.2$ (yellow dashed line), as noted previously for $Re = 70$. Moving to panel B, there is an overall decrease in peak Froude efficiency by about a factor of 2. The solid and dashed lines deviate more at larger l_y , as the now increased A/L results in more interaction between different horizontal rows of plates. For both lattice types, the peak Froude efficiency moves to much larger l_x . For larger A/L , the vorticity has a larger vertical extent. For an isolated plate, figure 7B shows that U/fA should be

kept roughly constant as A/L increases, for peak efficiency. This means that U/fL increases. Thus the vortices are more spread out horizontally, and it is reasonable that the plates should be more spread out to interact with vortices efficiently. The trend continues in panel C: a further reduction in peak Froude efficiency, that occurs at still larger l_x . In all cases, net thrust is obtained down to lower l_y by the rhombic lattice.

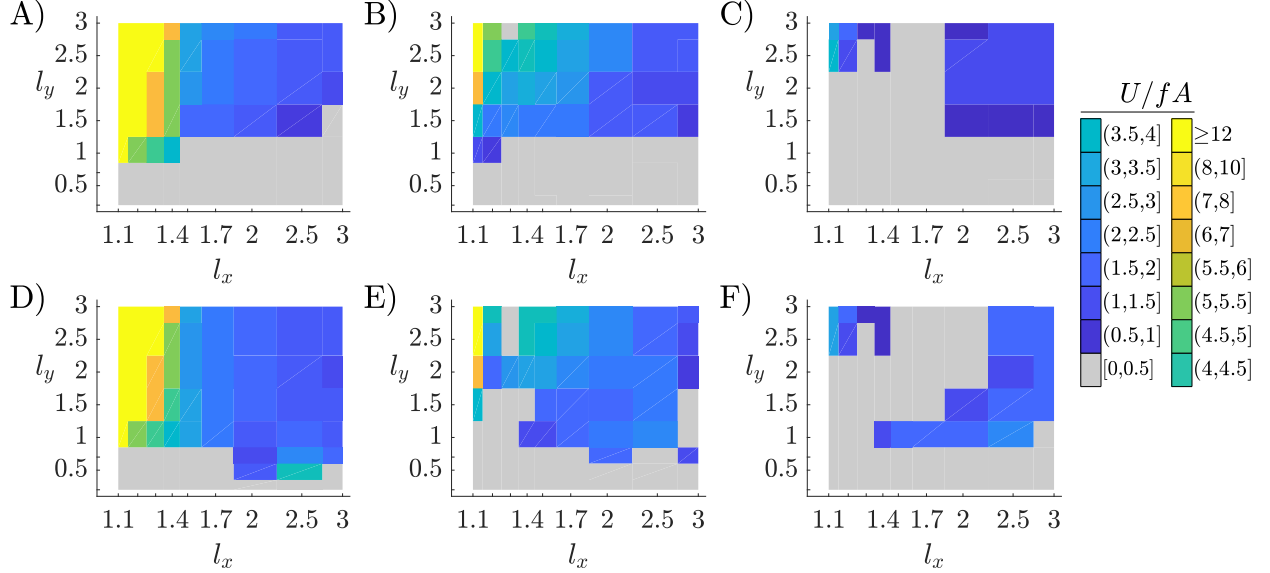


FIG. 21: Comparison of self-propelled speeds for rectangular (A-C) and rhombic (D-F) lattices at $Re = 20$ and $A/L = 0.2$ (A, D), 0.5 (B, E), and 0.8 (C, F).

Another measure of performance is the maximum self-propelled speed U_{SPS}/fA achieved by the lattice. These data are presented in figure 21 for the rectangular (top row) and rhombic (bottom row) lattices, at $A/L = 0.2, 0.5,$ and 0.8 (left to right columns). In all panels, the highest speeds are obtained at the smallest l_x , where vortex dipole formation leads to strong forces on the plates. The much smaller speeds at larger l_x may be partly due to the relatively small Re , which leads to substantial diffusion of vortices as they move over a larger lattice length scale. As in figure 20, the two lattices' speeds agree better at larger l_y ; the rhombic lattice achieves propulsion at smaller l_y than the rectangular lattice, with moderate to large l_x . An example is the local maximum in panel D at $l_x = 2.5$ and $l_y = 0.5$, close to the parameters for the flow in figure 19F but at lower Re . In panels B and E, there is a small band where $l_x = 1.3$ and $l_y = 2.5$ and 3 where the speed is greatly reduced or zero. The reason is not obvious, but may reflect a particular aspect of dipole formation at this value of Re .

When we increase Re much above 20, more flows are nonperiodic up to $t = 30$, and a contour plot of Froude efficiency like figure 20 would require much longer simulations to achieve reliable long-time averages. Therefore, for higher Re , we present data only for cases that meet a threshold for periodicity. We use the same criterion described in figure 14, but increase the threshold from 0.01 to 0.08. Even at this larger threshold, $F_x(t)$ is close to periodic. The larger threshold allows us to present more values, and observe the general trends more easily. These trends are not very sensitive to the particular threshold chosen (0.08). Figure 22 expands upon figure 21 by presenting peak Froude

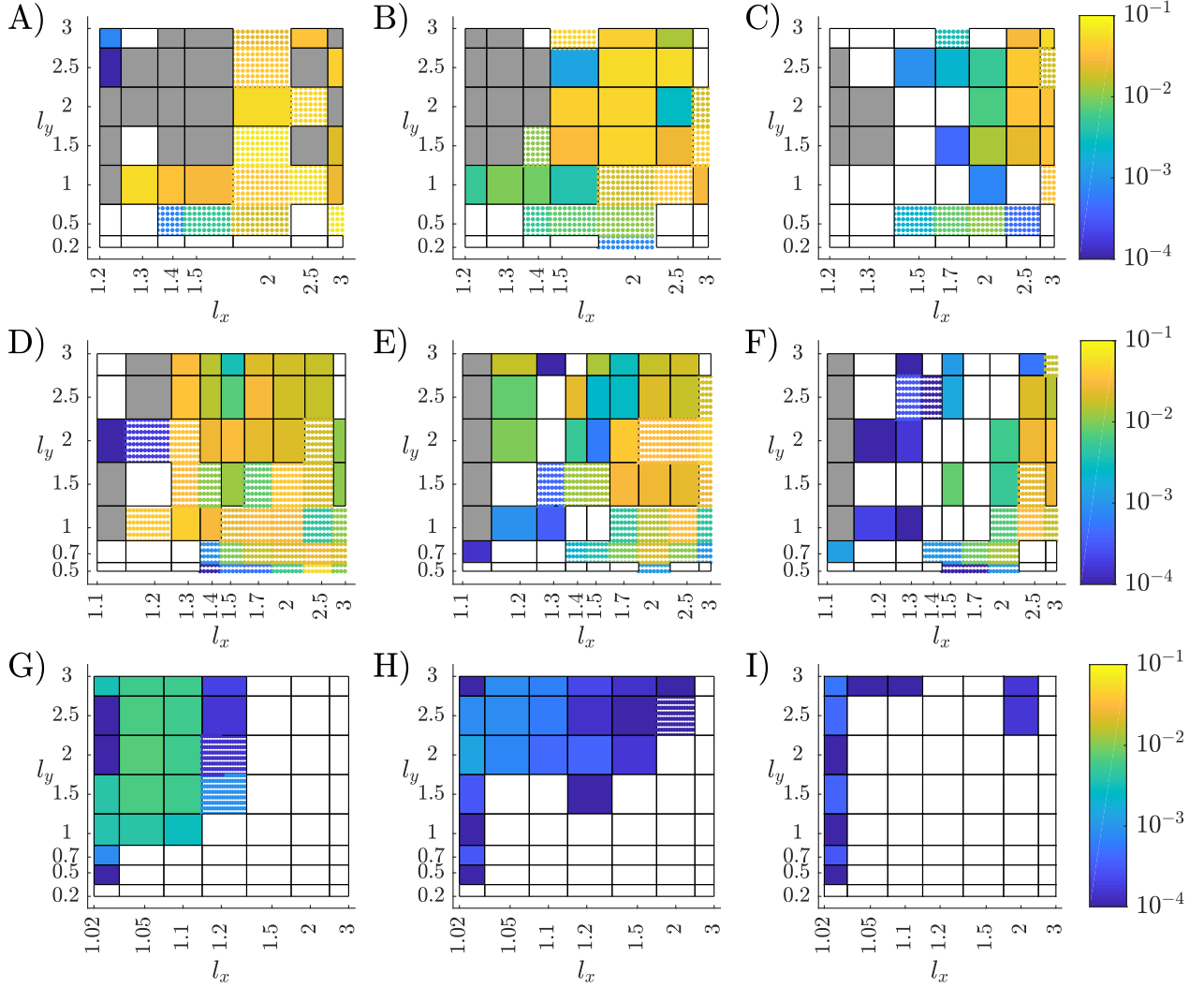


FIG. 22: Peak Froude efficiencies at $Re = 70$ (A-C), 40 (D-F), and 10 (G-I), for $A/L = 0.2$ (A,D,G), 0.5 (B,E,H), and 0.8 (C,F,I). White boxes denote only net drag is obtained. Gray boxes indicate that flows were nonperiodic across U/fA . White boxes indicate that flows were periodic at some U/fA , but these only produced net drag. Colored boxes indicate peak Froude efficiency magnitude (shown by color bars at right) where periodic flow(s) that produced net thrust occurred. The color field is solid or dotted if the peak was obtained with a rectangular or rhombic lattice, respectively. Each box is centered at the corresponding (l_x, l_y) value, except the boundary boxes, where the value is given at the corresponding boundary edge.

efficiency values for three Re : 70 (top row), 40 (middle row) and 10 (bottom row), with the same A/L , 0.2 , 0.5 , and 0.8 (left to right columns). We do not use contours now because in many cases, $F_x(t)$ is nonperiodic for all U/fA , and these are shown by gray boxes. If at a given choice of parameters there are U/fA such that $F_x(t)$ meets the criterion for periodicity, the color of the corresponding box denotes the peak Froude efficiency among the periodic cases, and the values are shown by the color bars at right. The box coloring is solid or dotted if the peak value is obtained with a rectangular or rhombic lattice, respectively. The white boxes are cases where there are periodic flows, but all such flows yield net drag. One basic trend is the increasing nonperiodicity of flows with Re : there are no gray boxes at Re

= 10, some at $\text{Re} = 40$, and more at $\text{Re} = 70$. Nonperiodicity is most common at small l_x , where the most intense vortex dipoles are created. At $\text{Re} = 70$, nonperiodicity is more common at smaller A/L , where Re_f is larger. At $\text{Re} = 10$ (bottom row), the highest efficiency states are found at the smallest l_x , which are taken as small as 1.02; periodic flows are obtained nonetheless due to the small Re . Consistent with figure 20, efficiency drops dramatically as A/L increases (from left to right). At $\text{Re} = 40$ (middle row), the most efficient periodic flows are obtained at much larger l_x . This is partly because many flows at smaller l_x are nonperiodic, however. At $\text{Re} = 40$ and 70 (top row), the basic trends of figure 20 are mostly preserved: rhombic lattice flows are most efficient at small l_y , rectangular lattice flows are usually more efficient at large l_y , and peak efficiencies move to larger l_x as A/L becomes larger (moving rightward). In general, as Re increases, so does peak Froude efficiency, from about 0.007 at $\text{Re} = 10$ to 0.033 at $\text{Re} = 20$ (from data in figure 20) to 0.055 at $\text{Re} = 40$, to 0.07 at $\text{Re} = 70$. As Re increases above 10, fewer and fewer states are periodic, so these should be regarded as conservative lower bounds for the true peak Froude efficiencies, ones that include long-time averages of nonperiodic flows.

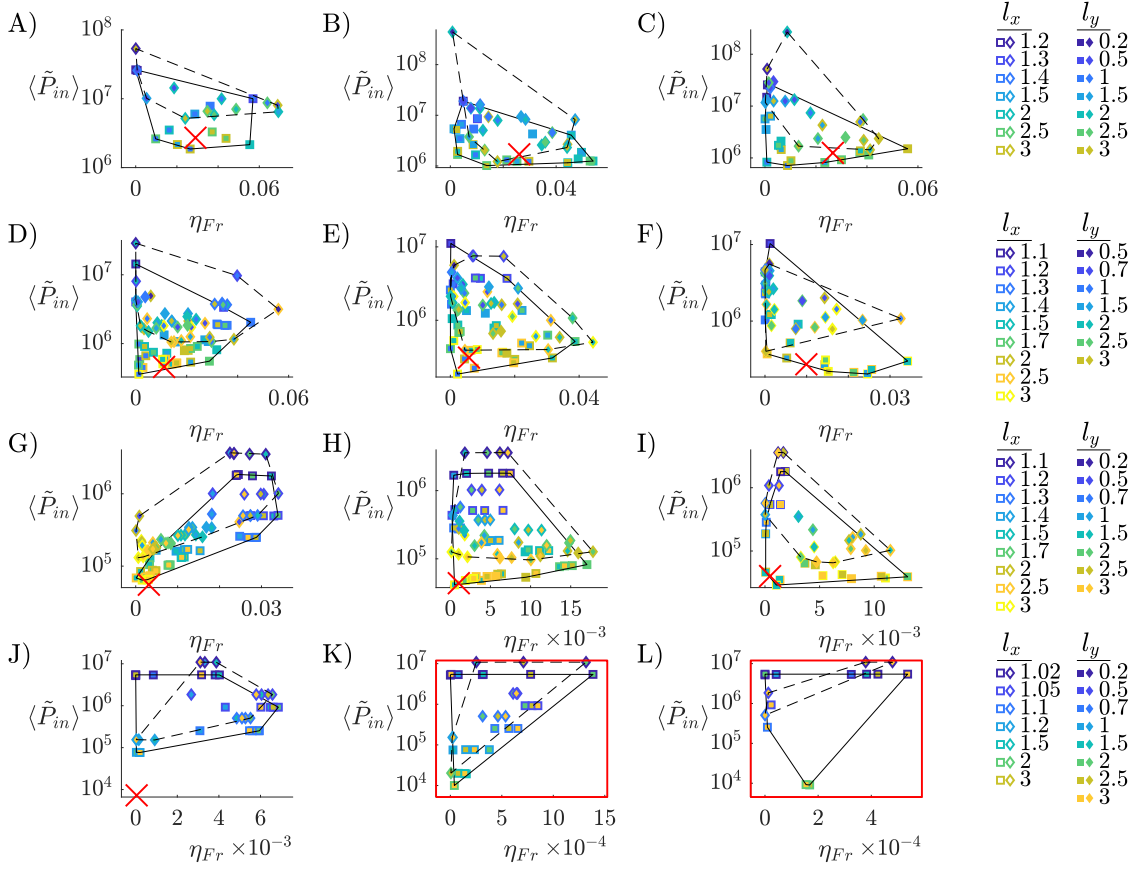


FIG. 23: Peak values of η_{Fr} versus $\langle \tilde{P}_{in} \rangle$ for rectangular (colored squares) and rhombic lattices (colored diamonds), at various l_x and l_y (colors at right). From top to bottom row, $\text{Re} = 70, 40, 20$, and 10. From left to right column, $A/L = 0.2, 0.5$, and 0.8.

We have shown in figure 22 how the maximum of the Froude efficiency over U/fA varies with respect to Re , A/L , l_x , and l_y for flows that are periodic or almost periodic. In figure 23 we replot the same data in figure 22, adding the

$Re = 20$ case, and showing both $\langle \tilde{P}_{in} \rangle$ and η_{Fr} simultaneously. Thus, the four rows from top to bottom correspond to $Re = 70, 40, 20,$ and 10 , while the three columns from left to right have $A/L = 0.2, 0.5,$ and 0.8 . This figure allows us to identify which configurations are effective at different input power budgets, and describe the Pareto frontier for this set of data. In each panel we plot the data for rectangular lattices with small squares, with convex hull shown as a solid black line. The data for rhombic lattices are small diamonds with convex hull shown as a dashed black line. For each data point, the outline color gives the value of l_x and the interior color gives the value of l_y (listed at right). In each panel we also plot, at the panel's values of Re and A/L , $\langle \tilde{P}_{in} \rangle$ and η_{Fr} for an isolated body. This is shown with a red cross, or if there is no thrust for the isolated body at any of the U/fA tested, the panel has a red outline. At the lowest two Re (bottom two rows), η_{Fr} for the isolated body is zero or much smaller than for the lattices. $\langle \tilde{P}_{in} \rangle$ for the isolated body is at the lower end of the range of lattice values, near the values for the largest l_x and l_y . Panel J is a somewhat special case, as the large- l_x lattice values did not yield thrust, but the isolated body did yield a very small net thrust—with η_{Fr} and $\langle \tilde{P}_{in} \rangle$ both much smaller than for the lattice values shown. For Re increased to 40 (second row from the top), there are lattice values with $\langle \tilde{P}_{in} \rangle$ lower than that of the isolated body, and some of these—rectangular lattices with large l_x and l_y —yield much higher efficiency. Moving to the top row ($Re = 70$), the isolated body's performance is relatively improved, lying near the middle of the range of lattice values. That is, the best periodic lattice flows have efficiencies about twice that of the isolated body. However, this should be regarded as only a lower bound on the efficiency advantage of the lattice flows. Many lattice flows were not counted due to nonperiodicity. These plots also show that input power for the rhombic lattices is generally larger than for the rectangular lattices, because the rhombic lattices cover more of the flow domain horizontally, forcing the fluid through smaller constrictions between the plates. Nonetheless, the largest η_{Fr} values here, in panel A, are for rhombic lattices. We also see that $\langle \tilde{P}_{in} \rangle$ is generally largest for smaller l_x and l_y (blue symbols) due to increased flow constriction, except that many of these cases are omitted because they have nonperiodic flows (especially in the top row).

Figure 24 shows the analogous plots when self-propelled speed (the maximum if there are multiple values) is substituted for Froude efficiency as the measure of performance on the horizontal axes. The self-propelled speed of the isolated body is less, but sometimes not much less, than the peak speeds of the lattices in the same panel. In some cases (panels A, F, G, and J), there is not a lattice flow that has larger $Re_{U,SPS}$ and smaller $\langle \tilde{P}_{in} \rangle$ simultaneously. However, this could easily change if temporally nonperiodic lattice flows were included.

VI. MEAN INPUT POWER

The Froude efficiency and self-propelled speed depend on how the mean horizontal force varies with oncoming flow speed. For a single flapping foil, this behavior depends on the physics of vortex creation and shedding due to large amplitude flapping at a given Reynolds number. Optimal vortex creation for thrust occurs when the foil moves a certain angle of attack in the flow; this motion can be computed but is difficult to describe with a simple analytical formula [98]. The same phenomenon underlies the prevalence and optimality of $St = 0.2$ – 0.4 for flapping locomotion at high Re [31, 34]. For a lattice of flapping bodies, the process is further complicated by the additional length scales

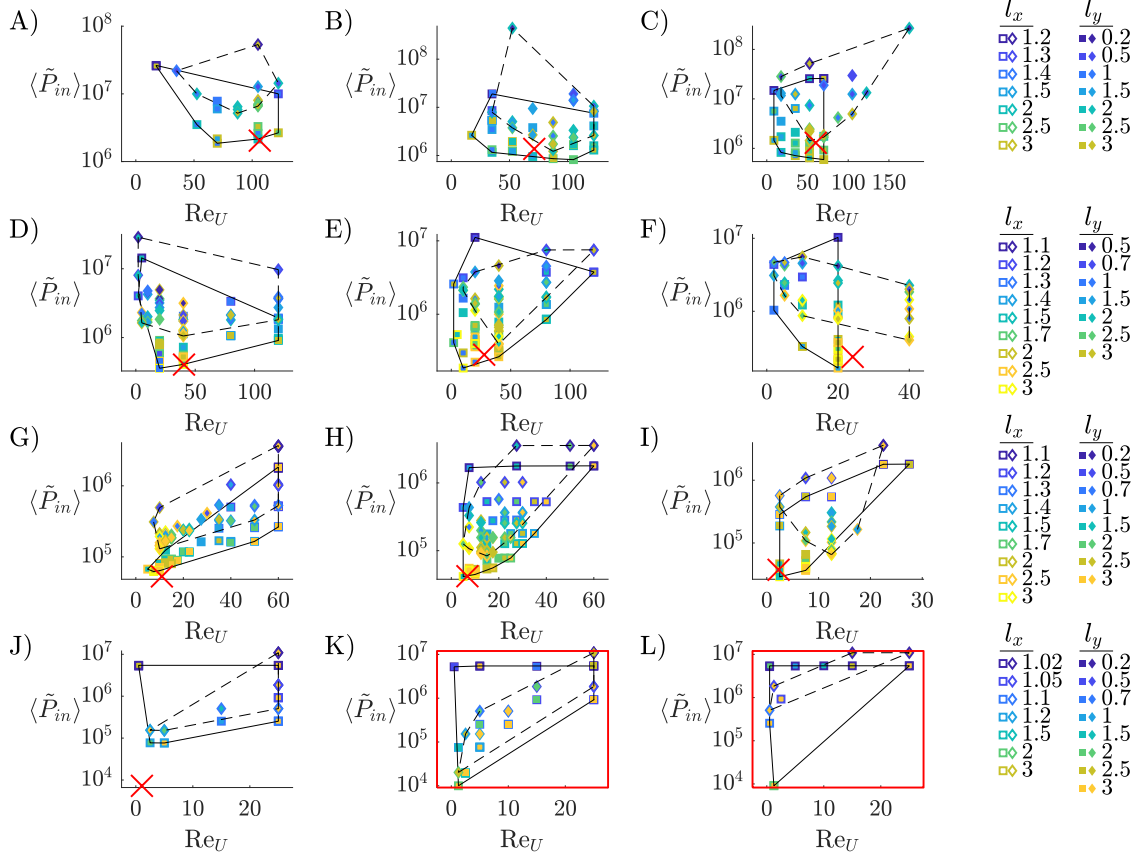


FIG. 24: Values of $Re_{U,SPS}$ versus $\langle \tilde{P}_{in} \rangle$ for rectangular (colored squares) and rhombic lattices (colored diamonds), at various l_x and l_y (colors at right). From top to bottom row, $Re = 70, 40, 20$, and 10 . From left to right column, $A/L = 0.2, 0.5$, and 0.8 .

of separation between bodies, and the effects of vortices colliding with downstream bodies.

One ingredient of Froude efficiency that is easier to address analytically is the time-averaged input power. We have seen in figure 9 for an isolated flapping plate that the mean input power scales as flapping amplitude and frequency cubed, and has a weaker dependence on the oncoming flow speed. This indicates perhaps that the dominant ingredient in the resistance of the fluid is the component of the plate's motion perpendicular to the plate. A simple model problem is steady flow through a lattice of plates at a given Reynolds number. For steady vertical flows, we nondimensionalize time by L/V , based on the (steady) spatial average of the vertical flow V (because there is no flapping frequency), giving a new definition of Reynolds number:

$$Re_V = VL/\nu. \quad (15)$$

Figure 25 shows steady vertical flows at $Re_V = 0.001$ through different types of lattices. For the rectangular lattice, there are two limiting regimes: $l_y/(l_x - 1) \ll 1$ (the ratio is $1/2$ in panel A) and $l_y/(l_x - 1) \gg 1$ (the ratio is 20 in panel B). The rhombic lattice has three limiting regimes. One is the same as panel B, $l_y/(l_x - 1) \gg 1$. Here the streamlines would be altered from those in B away from the gap between the plates, but would become the same

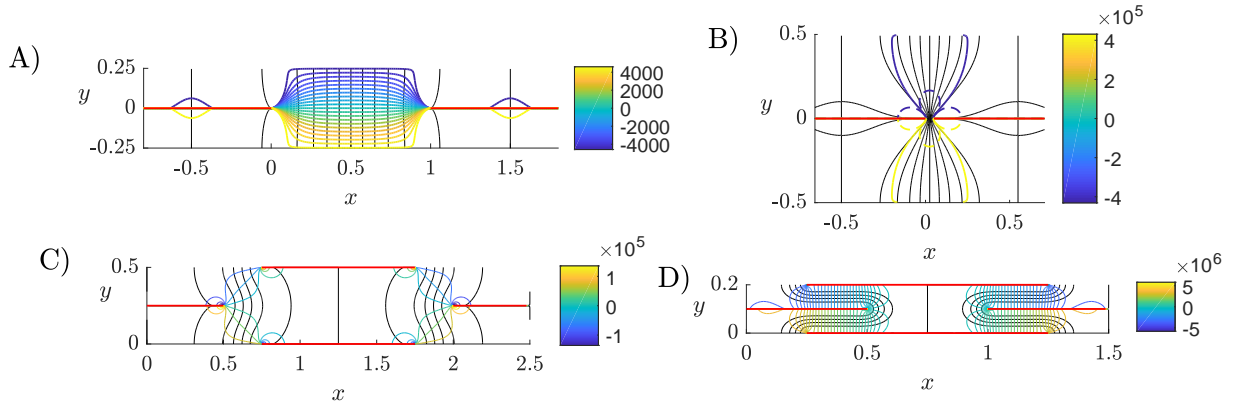


FIG. 25: Steady flows through plate lattices at $\text{Re}_V = 0.001$. Plates are red, streamlines are black, and isopressure lines are blue, green, and yellow (values in colorbars at right). A) Flow through rectangular lattice with $l_x = 2$ and $l_y = 0.5$. B) Flow through rectangular lattice with $l_x = 1.05$ and $l_y = 1$. C) Flow through rhombic lattice with $l_x = 2.5$ and $l_y = 0.25$. D) Flow through rhombic lattice with $l_x = 1.5$ and $l_y = 0.1$.

near the gap. The second is $l_y/(l_x/2 - 1) \ll 1$ with $l_x > 2$ (panel C has $l_y/(l_x/2 - 1) = 1$ and $l_x = 2.5$), and the third is $l_y/(1 - l_x/2) \ll 1$ with $l_x < 2$ (panel D has $l_y/(1 - l_x/2) = 0.4$ and $l_x = 1.5$). Only panel B is firmly in the asymptotic regime, while the other panels are at moderate ratios. In all cases, the flows resemble the limiting flows, even at moderate ratios.

The steady versions of equations (2)-(3) are

$$\mathbf{u} \cdot \nabla \mathbf{u} = -\nabla p + \frac{1}{\text{Re}_V} \nabla^2 \mathbf{u}, \quad (16)$$

$$\nabla \cdot \mathbf{u} = 0. \quad (17)$$

Integrating the y -component of (16) over a periodic unit cell, the left side vanishes because there is zero net vertical (or horizontal) outflow. So does the viscous term, because the inverse square root singularity in the shear stress diverges too slowly to produce a vertical resultant in the limit of zero plate thickness. Hence the integral of $-\partial_y p$ over the unit cell is zero. The integral has two contributions: one from the vertical change in p across the unit cell, and the other from the jump in p across the plate, resulting in a force applied by the plate to the fluid. Hence

$$0 = - \int_{\text{plate}} [p]_{-}^{+} dx - l_x l_y \frac{\Delta p_y}{l_y}, \quad (18)$$

where Δp_y is the change in pressure across the unit cell in the y direction. For the rhombic lattice, with two plates in a double unit cell (figure 1B), the integral in (18) includes both plates, and Δp_y is the change in pressure across the double unit cell in the y direction. For steady flow with dimensionless mean y -velocity 1,

$$\langle P_{in} \rangle = P_{in} = \int_{\text{plate}} [p]_{-}^{+} dx = -l_x \Delta p_y, \quad (19)$$

which relates the input power to the pressure difference across a unit cell in the y -direction. The latter can be determined analytically for the limiting cases of the flows in figure 25.

In the limit $l_y/(l_x - 1) \ll 1$, the flow in panel A becomes Poiseuille flow in the x -interval between the plate edges ($0 \leq x \leq 1$ in panel A), and zero flow in the rest of the flow field. Poiseuille flow is a good approximation to panel A even though $l_y/(l_x - 1) = 1/2$, not very small. The lack of streamlines above and below the plates indicates slow flow there (the local density of streamlines is proportional to flow speed). In the interval $0 \leq x \leq 1$ the flow is nearly unidirectional with a parabolic profile for $v(x)$, and the isopressure contours are nearly equally spaced, corresponding to the constant pressure gradient of Poiseuille flow. Using Poiseuille flow to relate the pressure gradient $\Delta p_y/l_y$ to the net fluid flux through the unit cell, $Q = 1 \cdot l_x$,

$$P_{in} = -l_x l_y \frac{\Delta p_y}{l_y} = l_x l_y \frac{12Q}{(l_x - 1)^3 \text{Re}_V} = \frac{12l_x^2}{(l_x - 1)^2 \text{Re}_V} \frac{l_y}{l_x - 1}. \quad (20)$$

The last expression in (20) is written in terms of $l_y/(l_x - 1)$, the parameter that sets the validity of the approximation.

The limit $l_y/(l_x - 1) \gg 1$ is exemplified by figure 25B. This is the Stokes flow through small gaps in a periodic array of plates. The black lines are again the streamlines. They show flow converging toward the gap, and a small recirculation region centered at the midpoints of the plates. To determine Δp_y and therefore P_{in} in (19), we can use the Stokes flow solution for a single gap in an infinite wall, derived by [105]. In the region that is much farther from the gap than its width, the pressure is approximately constant, one constant above the wall and a different constant below the wall. In figure 25B this is shown by the colored lines, isopressure contours (values at right). The solid line contours (dark blue and yellow) have pressures close to the values at distance 0.5 above and below the gaps (i.e. far from the gap). The dashed lines (dark blue and yellow) have pressures 1% above and below those of the solid lines. Hence, in panel B above and below the “cloverleaf” regions near the gap bounded by the dashed lines, the pressure varies by less than 2%. Therefore, the pressure field is essentially the same as that far from a single gap in an infinite wall. We approximate Δp_y in (19) as the difference between the far-field pressure constants for the infinite-wall case with net flux Q through the gap, from [105]: $\Delta p_y/Q = -32\text{Re}_V/(l_x - 1)^2\pi$. Then we have

$$P_{in} = -l_x \Delta p_y = \frac{32l_x^2}{\pi(l_x - 1)^2 \text{Re}_V}. \quad (21)$$

In figure 26 we plot P_{in} for steady flows through rectangular lattices. Each row shows data for a different value of Re_V , up to 6.4, close to the threshold at which the steady flow state becomes unstable for some choices of l_x close to 1. The first column shows P_{in} versus l_y for different choices of l_x (colored lines, values listed at right), at $U/V = 0$. The second column shows the same data in rescaled variables. P_{in} is divided by $l_x^2/(l_x - 1)^2 \text{Re}_V$, a factor that appears in both (20) and (21). On the horizontal axis, $l_y/(l_x - 1)$ is used as the dependent variable. The black line shows the Poiseuille flow scaling (20), while the black cross shows the value $32/\pi$ given by (21). The agreement is almost exact. The third and fourth columns show the same data for $U/V = 2$ and 8, respectively. Here the Poiseuille flow result (20) can be modified by including a dimensionless crossflow U/V in the flow equations [104], resulting in a $v(x)$ that is linear plus exponential. In place of (20) we obtain:

$$P_{in} = \frac{U}{V} l_x^2 l_y \left[\frac{l_x - 1}{\text{Re}_U} - \left(\frac{1}{2} + \frac{1}{e^{\text{Re}_U(l_x - 1)} - 1} \right) (l_x - 1)^2 \right]^{-1} \quad (22)$$

with $\text{Re}_U = UL/\nu$. P_{in} in (22) tends to (20) as $\text{Re}_U \rightarrow 0$, i.e. if either Re_V or $U/V \rightarrow 0$, so the crossflow has no effect in Stokes flow (as can also be seen by linearity). So only in the three panels near the lower right corner of figure

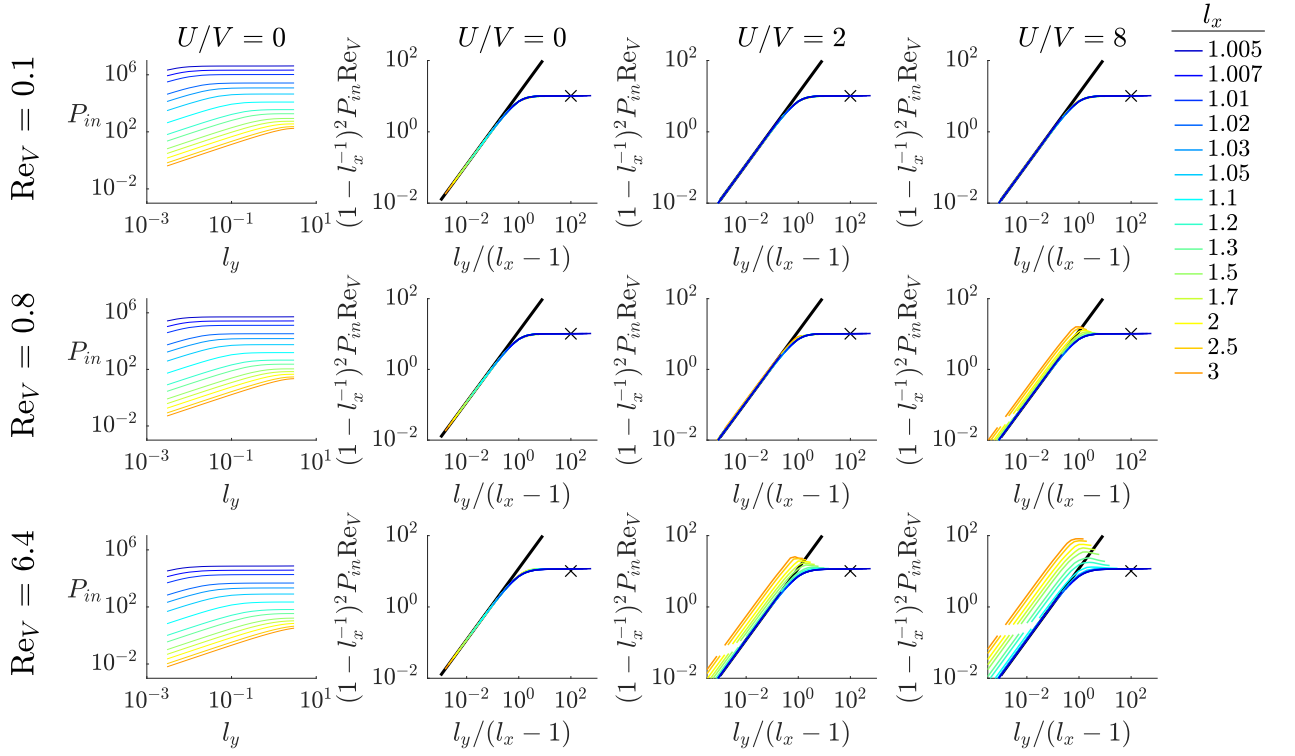


FIG. 26: For steady flow through a rectangular lattice, P_{in} versus l_y (left column) and in rescaled variables (second through fourth columns) for different values of Re_V (labeled at left) and U/V (labeled at top).

26—i.e the cases $(\text{Re}_V, U/V) = (0.8, 8)$, $(6.4, 2)$, and $(6.4, 8)$ —do the colored lines deviate noticeably from the black line; the deviation depends on l_x . The upper portions of the colored lines are the data computed from steady Navier-Stokes solutions and the lower portions (separated by a gap from the upper portions) are the Poiseuille-plus-crossflow approximations (22), different for each l_x , and which are linear in l_y . These line up almost exactly with the computed data. In summary, at small Re_V , P_{in} grows linearly with $l_y/(l_x - 1)$ when the ratio is small. The linear growth is because the rate of viscous energy dissipation per plate in the channel flows are proportional to the y -spacing between the plates, l_y . At large $l_y/(l_x - 1)$, P_{in} is independent of l_y because the small-gap flow, and the corresponding rate of viscous energy dissipation, becomes independent of l_y .

We now consider analytical models for the rhombic lattice, with examples of flows in figure 25C and D. The flow in panel C tends to two Poiseuille flows, each in a channel of width $l_x/2 - 1$, as $l_y/(l_x/2 - 1)$ becomes small. The flow in panel D tends to four Poiseuille flows, oriented horizontally, each in a channel of width l_y and length $1 - l_x/2$ (the horizontal overlap between the plates), as $l_y/(1 - l_x/2)$ becomes small. The pressure drop between the ends of the channels is half the total pressure drop over the double unit cell. The special case $l_x = 2$ and $l_y \rightarrow 0$, at the boundary between these flows, is more complicated and we do not address it here. Using these approximations, we obtain for

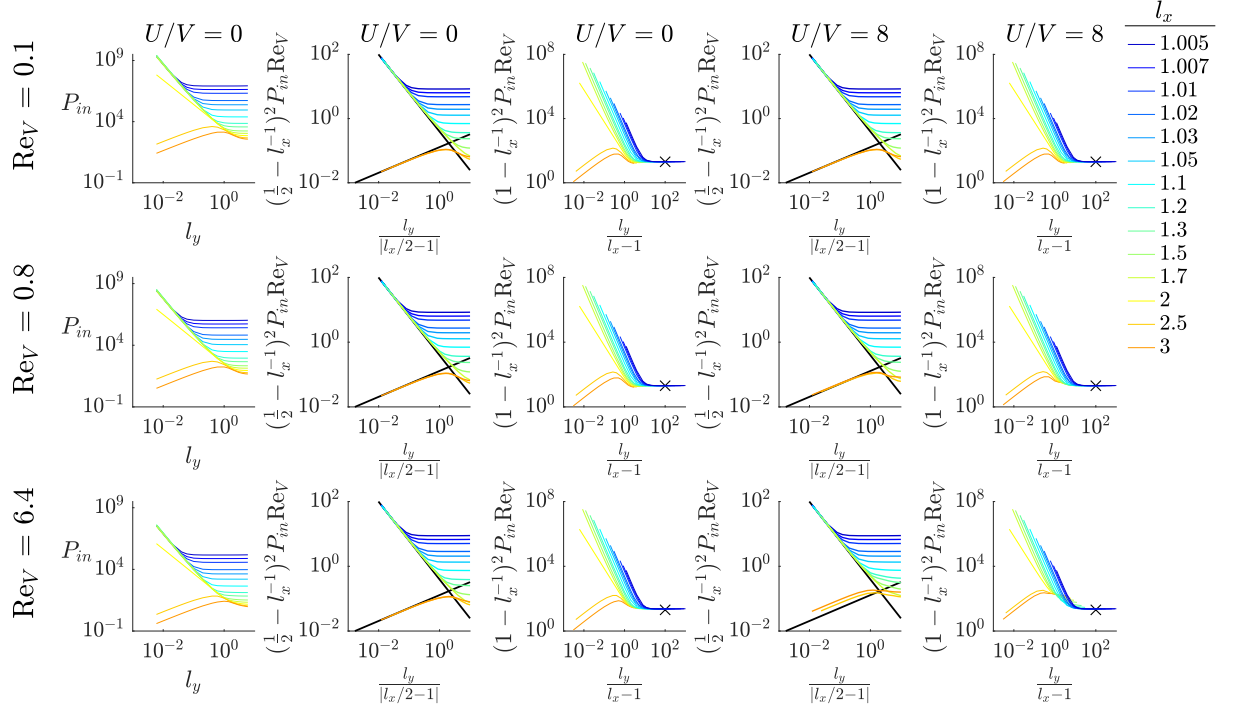


FIG. 27: For steady flow through a rhombic lattice, P_{in} versus l_y (left column) and in rescaled variables (second through fifth columns) for different values of Re_V (labeled at left) and U/V (labeled at top).

the limit $l_y/|l_x/2 - 1| \ll 1$,

$$P_{in} = \begin{cases} \frac{6l_x^2}{(l_x/2 - 1)^2 \text{Re}_V} \frac{l_y}{l_x/2 - 1}, & l_x > 2 \\ \frac{96l_x^2}{(1 - l_x/2)^2 \text{Re}_V} \left(\frac{1 - l_x/2}{l_y} \right)^3, & l_x < 2 \end{cases} \quad (23)$$

using the appropriate expressions for Δp_y . The case of large l_y is essentially the same as figure 25B, so for the double unit cell of the rhombic lattice, we have twice the P_{in} of (21). We compare these results with the computed steady Navier-Stokes results in figure 27. We use only two values of U/V now, 0 and 8, and the same Re_V as in figure 26. The first column shows the unscaled data at $U = 0$. Unlike for the rectangular lattice, the scaling of l_y changes from $l_y/|l_x/2 - 1|$ to $l_y/(l_x - 1)$ at small and large l_y respectively, so additional columns are needed to show the data with these separate scalings. The second and fourth columns show the small- l_y scalings, with black lines showing the relationships in (23). In the bottom panel of the fourth column ($(\text{Re}_V, U/V) = (6.4, 8)$), the colored lines with $l_x > 2$ are shifted at nonzero Re_U , due to the crossflow effect discussed for the rectangular lattice (not rederived here). There is no visible shift for the $l_x < 2$ lines, because the effect of the crossflow cancels for the four horizontal channel flows, two in each direction, in figure 25D. The black crosses (third and fifth columns) again show the large $l_y/(l_x - 1)$ values of P_{in} . The main difference from the rectangular lattice is the large growth in P_{in} at small l_y when $l_x < 2$. Propulsion occurs in many of these cases, e.g. at $l_y = 0.5$ and 0.7 (top and middle rows of figure 22). However, the peak Froude efficiency decreases noticeably when l_x drops below 2 and when l_y decreases in most of these cases.

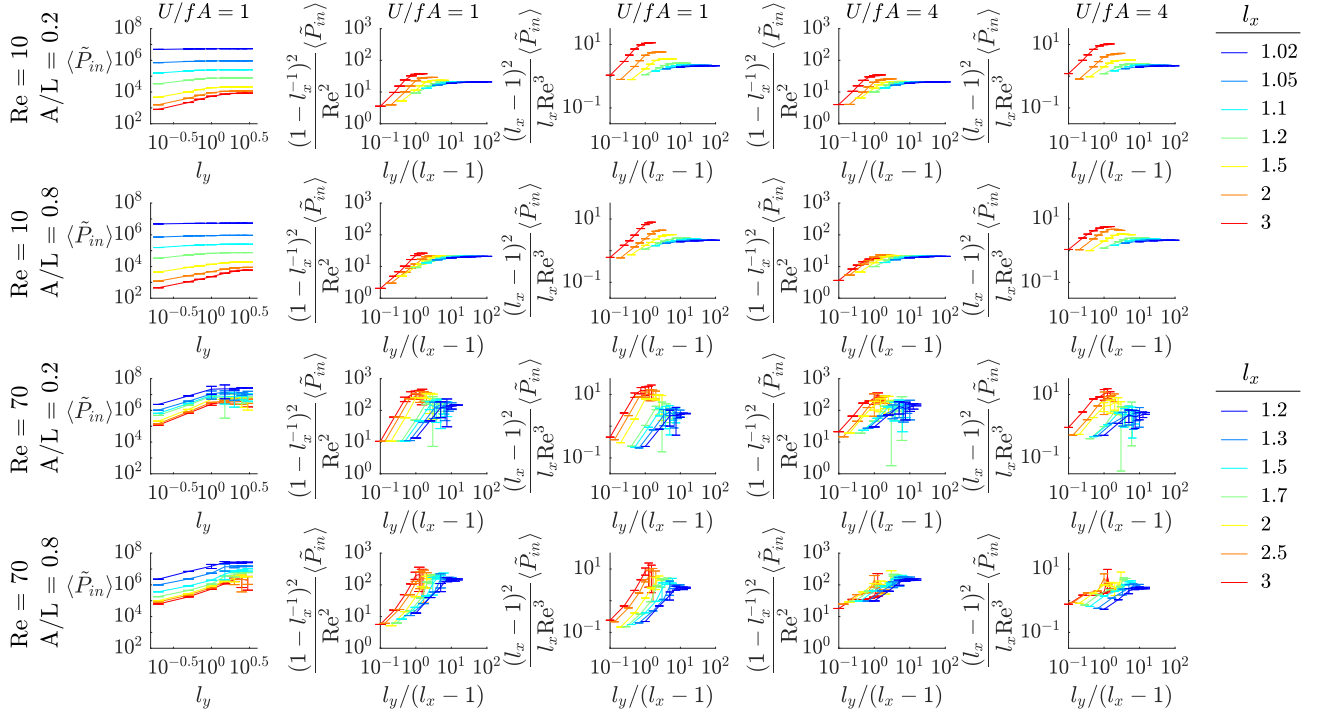


FIG. 28: Time-averaged input power $\langle \tilde{P}_{in} \rangle$ for flapping rectangular lattices at $U/fA = 1$ (first to third columns) and 4 (fourth and fifth columns), at $Re = 10$ and 70 and $A/L = 0.2$ and 0.8 (values labeled at left), for various l_x (listed separately for each Re at right). The error bars show the range of values within one standard deviation of $\langle \tilde{P}_{in} \rangle$. The standard deviation is computed using the last five period-averages of $\tilde{P}_{in}(t)$.

Now we consider the input power in the *unsteady*, fully nonlinear flapping problem, at $Re = 10$ – 70 . For the steady problem, the flows were plotted at much lower Reynolds number ($Re_V = 0.001$) in figure 25, mainly because an analytical solution is available in this limit for panel B, the small-gap case. However, the Poiseuille flows with a crossflow or without (as in panels A, C, and D) remain valid at larger Re_V , until they become unstable (at $Re_V = O(10^3)$ [131], above the Reynolds numbers in the present study). Nondimensionalizing (20) using ν/L in place of V , consistent with the unsteady $\langle \tilde{P}_{in} \rangle$ results in this paper, we have

$$\tilde{P}_{in} = \frac{12l_x^2}{(l_x - 1)^2} Re_V^2 \frac{l_y}{l_x - 1}. \quad (24)$$

The small-gap flow in panel B changes to a jet flow (e.g. figure 10) as the Reynolds number rises to 20. For $Re = 10$ – 70 the flow is intermediate between viscous-dominated (resulting in (21)) and inertia-dominated. In the latter case, the momentum theorem can be used to calculate \tilde{P}_{in} in the case of steady inertia-dominated (high- Re) flow. The calculation is the same as for the steady drag on an infinite, periodically perforated plate, given in [104], section 5.15. In the small-gap limit $l_y/(l_x - 1) \gg 1$, the pressure drop through a unit cell of our periodic lattice becomes the

same as that through the periodically perforated plate, which in our notation (and nondimensionalized by $\rho_f V^2$) is

$$\Delta p_y = -\frac{1}{2(l_x - 1)^2}. \quad (25)$$

The pressure is assumed to follow Bernoulli's law on the upstream sides of the plates, while on the downstream sides, where separated flow occurs, it is assumed constant and equal to that in the gap (see [104] for details). The input power follows from (19):

$$P_{in} = \frac{l_x}{2(l_x - 1)^2}; \tilde{P}_{in} = \frac{l_x}{2(l_x - 1)^2} \text{Re}_V^3. \quad (26)$$

where again, \tilde{P}_{in} has been nondimensionalized using ν/L in place of V , consistent with the unsteady results in this paper. For both Stokes flow (21) and separated flow (26) with small $l_x - 1$, P_{in} diverges like $(l_x - 1)^{-2}$, though with different prefactors.

Time-averaged input power for the rectangular lattice is plotted in figure 28 at two values of Re and A/L (labeled at left) and U/fA (labeled at top) in the ranges already considered. The unscaled $\langle \tilde{P}_{in} \rangle$ data are shown in the first column. $\langle \tilde{P}_{in} \rangle$ is rescaled according to the small- l_y Poiseuille flow scaling (24) in the second and fourth columns, and according to the large- l_y separated flow scaling (26) in the third and fifth columns, with Re (from (5)) in place of Re_V . The error bars show the range of values within one standard deviation of $\langle \tilde{P}_{in} \rangle$, computed using the last five period-averages of $\tilde{P}_{in}(t)$. In many cases (i.e. $\text{Re} = 10$, small l_y), $\tilde{P}_{in}(t)$ is periodic, so the error bar has almost zero height, and the upper and lower horizontal hash marks overlap, appearing as a single hash mark. At $\text{Re} = 70$ and larger l_y , the vertical extent of the error bar is noticeable, and gives a measure of the nonperiodicity of the data.

Although the data are more scattered in the unsteady case, they are qualitatively similar to the steady case (figure 26), including the shift at increasing l_x in the Poiseuille flow (linear growth regime). The steady problem neglected the effects of unsteadiness (an oscillating instead of steady vertical flow) and nonlinearity in the Navier-Stokes equations. We extended the steady model to the case of an unsteady but linearized model,

$$\partial_t v + U \partial_x v = -P_y e^{2\pi i t} + \frac{1}{\text{Re}_f} \partial_{xx} v, \quad (27)$$

for a harmonically oscillating channel flow $v(x, t) = V_0(x)e^{2\pi i t}$ with crossflow. Analytical solutions are again possible, but more complicated than the steady case because we are back in the five-dimensional parameter space. We did not analyze the results in detail but they seemed to agree qualitatively with the small l_y -results in figures 26 and 28. Despite the complications due to vortex shedding and nonperiodicity, the steady models and the fully nonlinear simulations agree qualitatively in the behavior of $\langle \tilde{P}_{in} \rangle$ —linear growth at small $l_y/(l_x - 1)$ in the second and fourth columns of figure 28, saturation at large $l_y/(l_x - 1)$ in the third and fifth columns. The main discrepancy is that the $\text{Re} = 10$ data have a larger magnitude than the $\text{Re} = 70$ data. A better fit is provided by the relation $\langle \tilde{P}_{in} \rangle \sim \text{Re}^3$ (typical for pressure losses at high Re , as in the third and fifth columns), rather than the $\sim \text{Re}^2$ scaling for steady Poiseuille flow used in the second and fourth columns of figure 28.

The fully nonlinear $\langle \tilde{P}_{in} \rangle$ data for the rhombic lattices are presented in figure 29. As for the rectangular lattices, the data are presented with different scalings at small l_y (second and fourth columns) and large l_y (third and fifth columns). In spite of the effects of nonperiodicity, there is good qualitative agreement between the unsteady and

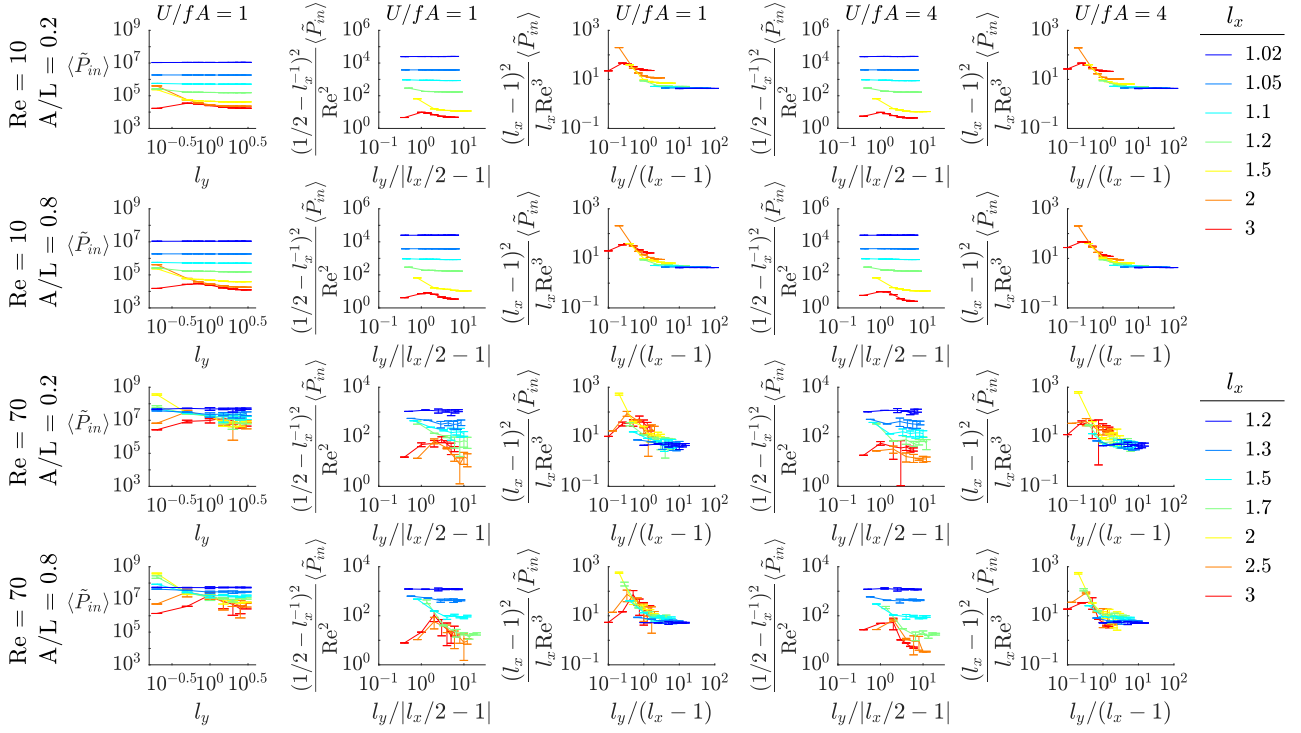


FIG. 29: Time-averaged input power $\langle \tilde{P}_{in} \rangle$ for flapping rhombic lattices at $U/fA = 1$ (first to third columns) and 4 (fourth and fifth columns), at $Re = 10$ and 70 and $A/L = 0.2$ and 0.8 (values labeled at left), for various l_x (listed separately for each Re at right). The error bars show the range of values within one standard deviation of $\langle \tilde{P}_{in} \rangle$. The standard deviation is computed using the last five period-averages of $\tilde{P}_{in}(t)$.

steady (figure 27) cases. In the second and fourth columns, there is a clear divergence at small $l_y/|l_x/2 - 1|$ between the lines with $l_x > 2$ (red and orange) and the remaining lines. We did not compute cases at $l_y/|l_x/2 - 1|$ as small as in figure 27, however, because they are not useful for locomotion, and in the unsteady case, the parameter space is larger and each simulation requires much more computing time. Again, the $Re = 10$ data are generally larger than the $Re = 70$ data in the second and fourth columns, perhaps indicating the importance of pressure losses beyond those of Poiseuille flow at higher Re . In the third and fifth columns, the lines at various l_x seem to agree reasonably well at large $l_y/(l_x - 1)$.

VII. SUMMARY AND CONCLUSIONS

We have studied propulsive properties of flapping lattices of plates, at $Re = 10$ – 100 , where the flows often become time-periodic within 5–30 flapping periods. This Re range is typical for submillimeter- to centimeter-scale flying and swimming organisms [96, 132–136], and is relevant to the increasing number of robotic flying and swimming vehicles that inhabit this size range [137–141]. Froude efficiency is typically much lower in this Re range than in the higher Re range typical of most fish and birds [5, 6, 10], so collective locomotion may be relatively more important for achieving

locomotion (efficiently, or at all, at very low Re where it is no longer possible for an isolated flapping body).

In our simulations, we used a rectilinear grid with grid points concentrated near the singularities at the plates' edges. The condition number of the discrete Laplacian remains many orders of magnitude below 10^{16} for the grids used in this paper, so round-off error is not a major obstacle. For a Laplace equation with similar singular behavior, we found that the method gives better than 1% accuracy in the solution and the integral of its gradient along the plate for modest mesh sizes, and converges at $3/2$ order.

We first used the method to determine the propulsive properties of an isolated flapping plate in this specific context (a plate with zero thickness flapping in a flow with fixed velocity upstream). The solutions show many properties that resemble those of previous flapping-foil studies: a reversed von Kármán street at certain oncoming flow speeds, more complicated vorticity fields at lower speeds, and a single stable self-propelled speed. The Strouhal numbers for maximal Froude efficiency increase from about 0.4 to $\gg 1$ as Re_f decreases from 200 to 10, while the Strouhal numbers corresponding to the self-propelled speeds increase from 0.25 to $\gg 1$ in the same range of Re_f . The maximum Froude efficiency for an isolated plate decreases from 0.06 at $Re_f = 200$ to less than 0.003 at $Re_f = 10$. These values are much lower than for higher- Re swimming fish and robots. This is consistent with the fact that flapping locomotion is not possible when Re decreases below a critical value close to 1, and there the maximum Froude efficiency becomes zero. The Pareto-optimal flapping amplitudes for maximizing speed at a given mean input power stay nearly fixed at 0.2–0.3. By contrast, the optimal flapping frequency increases with increasing self-propelled speed and/or input power. The input power scales as flapping amplitude and frequency, both raised to the third power, and depends only weakly on the oncoming flow velocity.

We then studied the propulsive properties of rectangular and rhombic lattices of flapping plates at low to moderate Reynolds numbers. Not surprisingly, there is a much wider range of flows than for an isolated body (which can also be regarded as the solution in the limit of large lattice spacing). When the plates are closely spaced in the streamwise direction (l_x close to 1), there are sharp transitions from drag to thrust with slight increases in the oncoming flow speed (U/fA). These correspond to changes in flow modes, characterized by vortex dipoles switching from upstream to downstream directions. Some of these flows have $F_x(t)$ with periods that are various integer multiples of half the flapping period, and others are nonperiodic. In general, nonperiodicity is more common at large Re , small l_x , large l_y , and small U/fA , for both rectangular and rhombic lattices, with more nonperiodicity at small l_y in the rhombic case.

As l_x increases beyond the vicinity of 1 with large l_y (akin to a 1D tandem array), the vortex dipoles transition to vortex-street wakes like those of isolated bodies, but which collide with the leading edges of plates downstream. Varying l_y from small to large with intermediate l_x (fixed at 2), the flows in rectangular and rhombic lattices are initially very different, with drag-producing Poiseuille-type flows in the rectangular case, and less periodic, thrust-producing flows in the rhombic case. Interactions between vorticity at laterally-adjacent leading and trailing edges in the rhombic lattices produced thrust efficiently at small l_y . As l_y increased, the rectangular lattice flows eventually shed discrete vortices and produced thrust, with somewhat higher efficiencies than the rhombic lattice in many cases.

We produced maps of maximum Froude efficiency and self-propelled speeds in different portions of the four-

dimensional (Re , A/L , l_x , l_y) parameter space where dynamics are close to periodic in time. At fixed Re , Froude efficiency is higher at $A/L = 0.2$ than at 0.5 and 0.8, and the peak occurs at gradually increasing l_x (and moderately large $l_y, \approx 2$) as A/L increases. The rhombic lattice is more efficient at small l_y , and the rectangular lattice is slightly more efficient in most cases at large l_y . The highest self-propelled speeds occurred at small l_x and large l_y for both lattice types. As Re was increased from 10 to 70, the peak Froude efficiency increased from 0.007 to 0.07. The isolated flapping body had a much lower Froude efficiency at $\text{Re} = 10$, eventually rising to about half that of the optimal lattices at $\text{Re} = 70$. However, many lattice flows are nonperiodic at $\text{Re} = 70$, and including these would increase the advantage over the isolated flapping body. The lattices showed similarly-sized advantages over the isolated bodies in the maximum self-propelled speeds.

The advantage in Froude efficiency occurs even with the much larger input power required for the lattices (due to the confinement of flow between the plates). In a steady model, we found that good analytical approximations to the input power could be derived for both lattice types. These relate to the flow through a small gap at small l_x and moderate l_y and Poiseuille flows with crossflow at small l_y and moderate l_x . The unsteady flows showed scaling behaviors that agreed qualitatively with those of the steady model flows.

To limit the number of parameters under consideration and the computational complexity, we have assumed all of the plates are moved together in phase (as in [71, 75] but not [42], for a small group of plates). Even with this restriction, varying the spacing between the plates gives us a degree of control of the phase between shed vortices and the motions of downstream bodies with which the vortices collide. In our study, the spacing between them is not allowed to vary with time (e.g. under fluid forces [71]). Incorporating these effects would greatly expand the parameter spaces under consideration but would be natural areas for future work.

Acknowledgments

This research was supported by the NSF Mathematical Biology program under award number DMS-1811889 (S.A.).

Appendix A: Appendix

Figure 30 shows examples of the vorticity fields at transitions in flows corresponding to the three sudden drops in $\langle F_x \rangle$ in figure 10D, as U/fA is increased slightly. In each case the vortex dipoles emitted from the gaps between the plates are oriented more downstream after the transition.

Figure 31 shows parameters where $F_x(t)$ falls below a threshold for periodicity in flows through rhombic lattices at $\text{Re} = 20$. Nonperiodicity is associated with small l_x , large l_y , and large St (small U/fA).

[1] M.J. Lighthill. Note on the swimming of slender fish. *J. Fluid Mech.*, 9(02):305–317, 1960.

[2] T.Y. Wu. Hydromechanics of swimming propulsion. Part 1. Swimming of a two-dimensional flexible plate at variable forward speeds in an inviscid fluid. *J. Fluid Mech.*, 46(2):337–355, 1971.

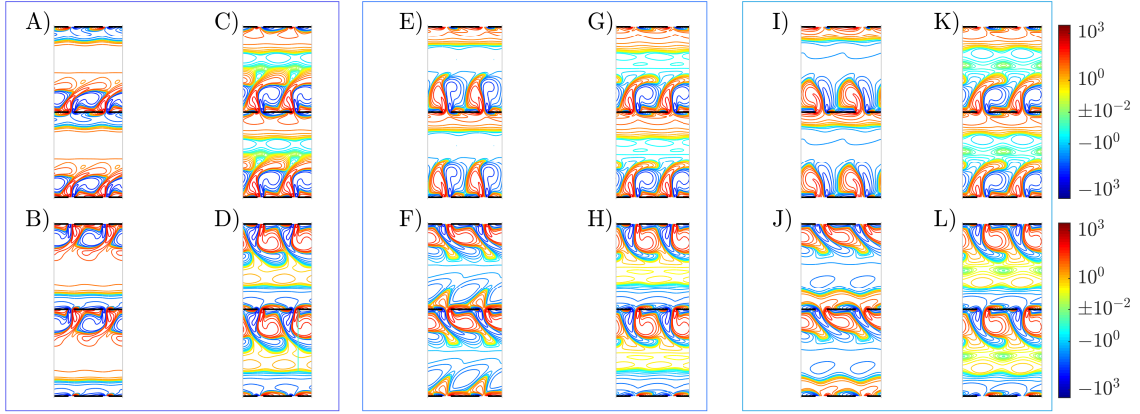


FIG. 30: Flow states that accompany each of the three sudden drops in $\langle F_x \rangle$ shown in figure 10D. In each case the flows transition from up-down asymmetric (panels A-B, E-F, and I-J) to symmetric (panels C-D, G-H, and K-L), with larger vortices downstream (rightward half of vortex dipoles). The first, second, and third boxes correspond to $l_x = 1.2, 1.3,$ and $1.4,$ respectively.

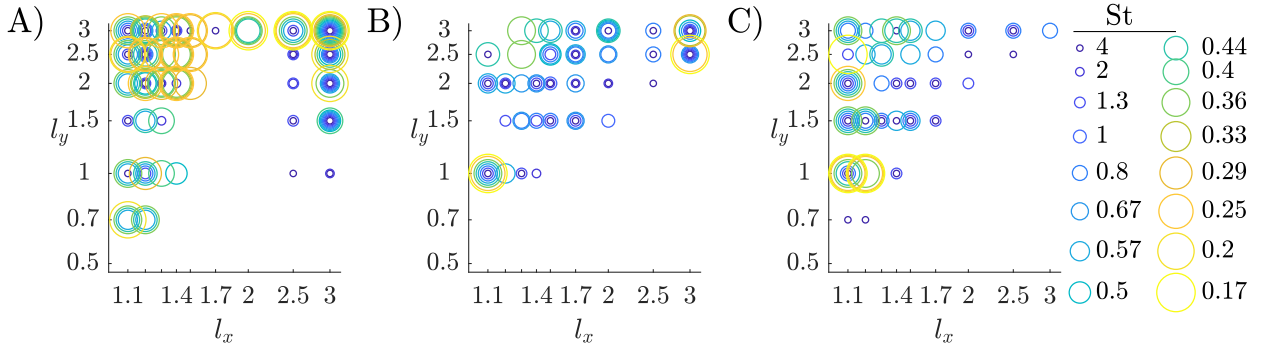


FIG. 31: Circles show parameter values where $F_x(t)$ falls below a threshold 0.01 (described in text adjacent to figure 14) for having period 1, for a rhombic lattice of plates with $Re = 20$. Values of A/L are 0.2 (A), 0.5 (B), and 0.8 (C). Values of St are labeled by circle size and color (key listed at right). Circles are centered at the corresponding values of l_x and l_y .

- [3] J.A. Sparenberg. *Hydrodynamic Propulsion and Its Optimization: Analytic Theory*. Springer, New York, 1995.
- [4] J.M. Anderson, K. Streitlien, D.S. Barrett, and M.S. Triantafyllou. Oscillating foils of high propulsive efficiency. *J. Fluid Mech.*, 360:41–72, 1998.
- [5] W. Shyy, M. Berg, and D. Ljungqvist. Flapping and flexible wings for biological and micro air vehicles. *Prog. Aero. Sci.*, 35:455–505, 1999.
- [6] M.S. Triantafyllou, G.S. Triantafyllou, and D.K.P. Yue. Hydrodynamics of fishlike swimming. *Annu. Rev. Fluid Mech.*, 32:33–53, 2000.
- [7] G. C. Lewin and H. Haj-hariri. Modelling thrust generation of a two-dimensional heaving airfoil in a viscous flow. *J. Fluid Mech.*, 492:339–362, 2003.
- [8] M.S. Triantafyllou, A.H. Techet, and F.S. Hover. Review of experimental work in biomimetic foils. *Oceanic Engineering, IEEE Journal of*, 29(3):585–594, 2004.
- [9] S. Heathcote and I. Gursul. Flexible Flapping Airfoil Propulsion at Low Reynolds Numbers. *AIAA Paper*, 1405:2005, 2005.

- [10] Frank Fish and George V Lauder. Passive and active flow control by swimming fishes and mammals. *Annu. Rev. Fluid Mech.*, 38:193–224, 2006.
- [11] Laura A Miller, Daniel I Goldman, Tyson L Hedrick, Eric D Tytell, Z Jane Wang, Jeannette Yen, and Silas Alben. Using computational and mechanical models to study animal locomotion, 2012.
- [12] Alexander J Smits. Undulatory and oscillatory swimming. *Journal of Fluid Mechanics*, 874, 2019.
- [13] P Freymuth. Propulsive vortical signature of plunging and pitching airfoils. *AIAA J.*, 26(7):881–883, Jul. 1988.
- [14] KD Von Ellenrieder, K Parker, and J Soria. Flow structures behind a heaving and pitching finite-span wing. *J. Fluid Mech.*, 490:129–138, Sep. 2003.
- [15] James HJ Buchholz and Alexander J Smits. On the evolution of the wake structure produced by a low-aspect-ratio pitching panel. *Journal of fluid mechanics*, 564:433, 2005.
- [16] S. Alben. Optimal flexibility of a flapping appendage at high Reynolds number. *J. Fluid Mech.*, 614:355–380, 2008.
- [17] S. Michelin and S.G.L. Smith. Resonance and propulsion performance of a heaving flexible wing. *Physics of Fluids*, 21:071902, 2009.
- [18] S. Alben. Simulating the dynamics of flexible bodies and vortex sheets. *J. Comp. Phys.*, 228(7):2587–2603, 2009.
- [19] Peter Derek Yeh and Alexander Alexeev. Free swimming of an elastic plate plunging at low reynolds number. *Physics of Fluids*, 26(5):053604, 2014.
- [20] Alexander P Hoover, Ricardo Cortez, Eric D Tytell, and Lisa J Fauci. Swimming performance, resonance and shape evolution in heaving flexible panels. *Journal of Fluid Mechanics*, 847:386–416, 2018.
- [21] Andrew Hess, Xiaobo Tan, and Tong Gao. Cfd-based multi-objective controller optimization for soft robotic fish with muscle-like actuation. *Bioinspiration & Biomimetics*, 15(3):035004, 2020.
- [22] Eric D Tytell, Megan C Leftwich, Chia-Yu Hsu, Boyce E Griffith, Avis H Cohen, Alexander J Smits, Christina Hamlet, and Lisa J Fauci. Role of body stiffness in undulatory swimming: insights from robotic and computational models. *Physical Review Fluids*, 1(7):073202, 2016.
- [23] Tingyu Ming, Bowen Jin, Jialei Song, Haoxiang Luo, Ruxu Du, and Yang Ding. 3d computational models explain muscle activation patterns and energetic functions of internal structures in fish swimming. *PLoS computational biology*, 15(9):e1006883, 2019.
- [24] Nicolas Vandenberghe, Jun Zhang, and Stephen Childress. Symmetry breaking leads to forward flapping flight. *Journal of Fluid Mechanics*, 506:147–155, 2004.
- [25] Silas Alben and Michael Shelley. Coherent locomotion as an attracting state for a free flapping body. *Proceedings of the National Academy of Sciences*, 102(32):11163–11166, 2005.
- [26] Saverio E Spagnolie, Lionel Moret, Michael J Shelley, and Jun Zhang. Surprising behaviors in flapping locomotion with passive pitching. *Physics of Fluids*, 22(4):041903, 2010.
- [27] Silas Alben, Charles Witt, T Vernon Baker, Erik Anderson, and George V Lauder. Dynamics of freely swimming flexible foils. *Physics of Fluids*, 24(5):051901, 2012.
- [28] M.J. Shelley and J. Zhang. Flapping and Bending Bodies Interacting with Fluid Flows. *Annual Review of Fluid Mechanics*, 43:449–465, 2011.
- [29] G.S. Triantafyllou, M.S. Triantafyllou, and M.A. Grosenbaugh. Optimal thrust development in oscillating foils with application to fish propulsion. *J. Fluids Struct.*, 7:205–224, 1993.
- [30] K.D. Jones, C.M. Dohring, and M.F. Platzer. An experimental and computational investigation of the Knoller-Betz effect. *AIAA J.*, 36:1240–1246, 1998.

- [31] G.K. Taylor, R.L. Nudds, and A.L.R. Thomas. Flying and swimming animals cruise at a strouhal number tuned for high power efficiency. *Nature*, 425:707–711, 2003.
- [32] Jim J Rohr and Frank E Fish. Strouhal numbers and optimization of swimming by odontocete cetaceans. *Journal of Experimental Biology*, 207(10):1633–1642, 2004.
- [33] John O Dabiri. Optimal vortex formation as a unifying principle in biological propulsion. *Annual review of fluid mechanics*, 41:17–33, 2009.
- [34] Christophe Eloy. Optimal strouhal number for swimming animals. *Journal of Fluids and Structures*, 30:205–218, 2012.
- [35] Ramiro Godoy-Diana, Jean-Luc Aider, and José Eduardo Wesfreid. Transitions in the wake of a flapping foil. *Physical Review E*, 77(1):016308, 2008.
- [36] Teis Schnipper, Anders Andersen, and Tomas Bohr. Vortex wakes of a flapping foil. *Journal of Fluid Mechanics*, 633:411, 2009.
- [37] JA Sparenberg and AK Wiersma. On the efficiency increasing interaction of thrust producing lifting surfaces. In *Swimming and flying in nature*, pages 891–917. Springer, 1975.
- [38] Imran Akhtar, Rajat Mittal, George V Lauder, and Elliot Drucker. Hydrodynamics of a biologically inspired tandem flapping foil configuration. *Theoretical and Computational Fluid Dynamics*, 21(3):155–170, 2007.
- [39] Z Jane Wang and David Russell. Effect of forewing and hindwing interactions on aerodynamic forces and power in hovering dragonfly flight. *Physical review letters*, 99(14):148101, 2007.
- [40] Birgitt M Boschitsch, Peter A Dewey, and Alexander J Smits. Propulsive performance of unsteady tandem hydrofoils in an in-line configuration. *Physics of Fluids*, 26(5):051901, 2014.
- [41] Melike Kurt and Keith W Moored. Flow interactions of two-and three-dimensional networked bio-inspired control elements in an in-line arrangement. *Bioinspiration & biomimetics*, 13(4):045002, 2018.
- [42] Xingjian Lin, Jie Wu, Tongwei Zhang, and Liming Yang. Phase difference effect on collective locomotion of two tandem autopropelled flapping foils. *Physical Review Fluids*, 4(5):054101, 2019.
- [43] David Rival, Guillermo Hass, and Cameron Tropea. Recovery of energy from leading-and trailing-edge vortices in tandem-airfoil configurations. *Journal of Aircraft*, 48(1):203–211, 2011.
- [44] K. Streitlien, G.S. Triantafyllou, and M.S. Triantafyllou. Efficient foil propulsion through vortex control. *AIAA J.*, 34(11):2315–2319, 1996.
- [45] James C Liao, David N Beal, George V Lauder, and Michael S Triantafyllou. Fish exploiting vortices decrease muscle activity. *Science*, 302(5650):1566–1569, 2003.
- [46] DN Beal, FS Hover, MS Triantafyllou, JC Liao, and GV Lauder. Passive propulsion in vortex wakes. *Journal of Fluid Mechanics*, 549:385–402, 2006.
- [47] James C Liao. A review of fish swimming mechanics and behaviour in altered flows. *Philosophical Transactions of the Royal Society B: Biological Sciences*, 362(1487):1973–1993, 2007.
- [48] S. Alben. On the swimming of a flexible body in a vortex street. *Journal of Fluid Mechanics*, 635:27–45, 2009.
- [49] S. Alben. Passive and active bodies in vortex-street wakes. *Journal of Fluid Mechanics*, 642:95–125, 2009.
- [50] TL Doligalski, CR Smith, and JDA Walker. Vortex interactions with walls. *Annual Review of Fluid Mechanics*, 26(1):573–616, 1994.
- [51] Donald Rockwell. Vortex-body interactions. *Annual review of fluid mechanics*, 30(1):199–229, 1998.
- [52] Silas Alben. Interactions between vortices and flexible walls. *International Journal of Non-Linear Mechanics*, 46(4):586–591, 2011.

- [53] S. Alben. The attraction between a flexible filament and a point vortex. *Journal of Fluid Mechanics*, 697:481–503, 2012.
- [54] Brooke E Flammang, Silas Alben, Peter GA Madden, and George V Lauder. Functional morphology of the fin rays of teleost fishes. *Journal of morphology*, 274(9):1044–1059, 2013.
- [55] Daniel B Quinn, Keith W Moored, Peter A Dewey, and Alexander J Smits. Unsteady propulsion near a solid boundary. *Journal of Fluid Mechanics*, 742:152, 2014.
- [56] L. Ristroph and J. Zhang. Anomalous Hydrodynamic Drafting of Interacting Flapping Flags. *Physical Review Letters*, 101(19), 2008.
- [57] Luoding Zhu. Interaction of two tandem deformable bodies in a viscous incompressible flow. *Journal of Fluid Mechanics*, 635:455, 2009.
- [58] Silas Alben. Wake-mediated synchronization and drafting in coupled flags. *Journal of Fluid Mechanics*, 641:489–496, 2009.
- [59] Sohae Kim, Wei-Xi Huang, and Hyung Jin Sung. Constructive and destructive interaction modes between two tandem flexible flags in viscous flow. *Journal of Fluid Mechanics*, 661:511, 2010.
- [60] Emad Uddin, Wei-Xi Huang, and Hyung Jin Sung. Interaction modes of multiple flexible flags in a uniform flow. *Journal of Fluid Mechanics*, 729:563–583, 2013.
- [61] David Lentink, GertJan F Van Heijst, Florian T Muijres, and Johan L Van Leeuwen. Vortex interactions with flapping wings and fins can be unpredictable. *Biology Letters*, 6(3):394–397, 2010.
- [62] Gen Li, Dmitry Kolomenskiy, Hao Liu, Benjamin Thiria, and Ramiro Godoy-Diana. On the energetics and stability of a minimal fish school. *PloS one*, 14(8), 2019.
- [63] Christopher Dombrowski, Luis Cisneros, Sunita Chatkaew, Raymond E Goldstein, and John O Kessler. Self-concentration and large-scale coherence in bacterial dynamics. *Physical review letters*, 93(9):098103, 2004.
- [64] David Saintillan and Michael J Shelley. Instabilities and pattern formation in active particle suspensions: kinetic theory and continuum simulations. *Physical Review Letters*, 100(17):178103, 2008.
- [65] Eric Lauga and Thomas R Powers. The hydrodynamics of swimming microorganisms. *Reports on Progress in Physics*, 72(9):096601, 2009.
- [66] Donald L Koch and Ganesh Subramanian. Collective hydrodynamics of swimming microorganisms: living fluids. *Annual Review of Fluid Mechanics*, 43:637–659, 2011.
- [67] Jens Elgeti, Roland G Winkler, and Gerhard Gompper. Physics of microswimmers: single particle motion and collective behavior: a review. *Reports on progress in physics*, 78(5):056601, 2015.
- [68] David Saintillan. Rheology of active fluids. *Annual Review of Fluid Mechanics*, 50:563–592, 2018.
- [69] Sara Pålsson and Anna-Karin Tornberg. An integral equation method for closely interacting surfactant-covered droplets in wall-confined stokes flow. *International Journal for Numerical Methods in Fluids*, 2020.
- [70] Bowei Wu, Hai Zhu, Alex Barnett, and Shravan Veerapaneni. Solution of stokes flow in complex nonsmooth 2d geometries via a linear-scaling high-order adaptive integral equation scheme. *Journal of Computational Physics*, page 109361, 2020.
- [71] Alexander D Becker, Hassan Masoud, Joel W Newbolt, Michael Shelley, and Leif Ristroph. Hydrodynamic schooling of flapping swimmers. *Nature communications*, 6(1):1–8, 2015.
- [72] Sophie Ramanarivo, Fang Fang, Anand Oza, Jun Zhang, and Leif Ristroph. Flow interactions lead to orderly formations of flapping wings in forward flight. *Physical Review Fluids*, 1(7):071201, 2016.
- [73] Longzhen Dai, Guowei He, Xiang Zhang, and Xing Zhang. Stable formations of self-propelled fish-like swimmers induced by hydrodynamic interactions. *Journal of The Royal Society Interface*, 15(147):20180490, 2018.

- [74] Seyedsaeed Mirazimi. *Meso-swimmer suspensions: immersed boundary simulations of hydrodynamic interactions between worm-like swimmers*. PhD thesis, Science: Department of Mathematics, 2018.
- [75] Ze-Rui Peng, Haibo Huang, and Xi-Yun Lu. Hydrodynamic schooling of multiple self-propelled flapping plates. *Journal of Fluid Mechanics*, 853:587–600, 2018.
- [76] Ze-Rui Peng, Haibo Huang, and Xi-Yun Lu. Collective locomotion of two closely spaced self-propelled flapping plates. *Journal of Fluid Mechanics*, 849:1068–1095, 2018.
- [77] Sunghyuk Im, Sung Goon Park, Yeunwoo Cho, and Hyung Jin Sung. Schooling behavior of rigid and flexible heaving airfoils. *International Journal of Heat and Fluid Flow*, 69:224–233, 2018.
- [78] Anand U Oza, Leif Ristroph, and Michael J Shelley. Lattices of hydrodynamically interacting flapping swimmers. *Physical Review X*, 9(4):041024, 2019.
- [79] Joel W Newbolt, Jun Zhang, and Leif Ristroph. Flow interactions between uncoordinated flapping swimmers give rise to group cohesion. *Proceedings of the National Academy of Sciences*, 116(7):2419–2424, 2019.
- [80] Daniel Weihs. Some hydrodynamical aspects of fish schooling. In *Swimming and flying in nature*, pages 703–718. Springer, 1975.
- [81] BL Partridge and TJ Pitcher. Evidence against a hydrodynamic function for fish schools. *Nature*, 279(5712):418–419, 1979.
- [82] Jon C Svendsen, Jakob Skov, Mogens Bildsoe, and John Fleng Steffensen. Intra-school positional preference and reduced tail beat frequency in trailing positions in schooling roach under experimental conditions. *Journal of fish biology*, 62(4):834–846, 2003.
- [83] Steven J Portugal, Tatjana Y Hubel, Johannes Fritz, Stefanie Heese, Daniela Trobe, Bernhard Voelkl, Stephen Hailes, Alan M Wilson, and James R Usherwood. Upwash exploitation and downwash avoidance by flap phasing in ibis formation flight. *Nature*, 505(7483):399–402, 2014.
- [84] Mohsen Daghooghi and Iman Borazjani. The hydrodynamic advantages of synchronized swimming in a rectangular pattern. *Bioinspiration & biomimetics*, 10(5):056018, 2015.
- [85] Stefano Marras, Shaun S Killen, Jan Lindström, David J McKenzie, John F Steffensen, and Paolo Domenici. Fish swimming in schools save energy regardless of their spatial position. *Behavioral ecology and sociobiology*, 69(2):219–226, 2015.
- [86] CK Hemelrijk, DAP Reid, H Hildenbrandt, and JT Padding. The increased efficiency of fish swimming in a school. *Fish and Fisheries*, 16(3):511–521, 2015.
- [87] Nick Gravish, Jacob M Peters, Stacey A Combes, and Robert J Wood. Collective flow enhancement by tandem flapping wings. *Physical review letters*, 115(18):188101, 2015.
- [88] Gaojin Li, Anca Ostace, and Arezoo M Ardekani. Hydrodynamic interaction of swimming organisms in an inertial regime. *Physical Review E*, 94(5):053104, 2016.
- [89] Muhammad Saif Ullah Khalid, Imran Akhtar, and Haibo Dong. Hydrodynamics of a tandem fish school with asynchronous undulation of individuals. *Journal of Fluids and Structures*, 66:19–35, 2016.
- [90] Intesaaf Ashraf, Hanaé Bradshaw, Thanh-Tung Ha, José Halloy, Ramiro Godoy-Diana, and Benjamin Thiria. Simple phalanx pattern leads to energy saving in cohesive fish schooling. *Proceedings of the National Academy of Sciences*, 114(36):9599–9604, 2017.
- [91] Sung Goon Park and Hyung Jin Sung. Hydrodynamics of flexible fins propelled in tandem, diagonal, triangular and diamond configurations. *Journal of Fluid Mechanics*, 840:154–189, 2018.

- [92] Mattia Gazzola, Andrew A Tchieu, Dmitry Alexeev, Alexia de Brauer, and Petros Koumoutsakos. Learning to school in the presence of hydrodynamic interactions. *Journal of Fluid Mechanics*, 789:726–749, 2016.
- [93] Guido Novati, Siddhartha Verma, Dmitry Alexeev, Diego Rossinelli, Wim M Van Rees, and Petros Koumoutsakos. Synchronisation through learning for two self-propelled swimmers. *Bioinspiration & biomimetics*, 12(3):036001, 2017.
- [94] Yael Katz, Kolbjørn Tunstrøm, Christos C Ioannou, Cristián Huepe, and Iain D Couzin. Inferring the structure and dynamics of interactions in schooling fish. *Proceedings of the National Academy of Sciences*, 108(46):18720–18725, 2011.
- [95] Audrey Filella, François Nadal, Clément Sire, Eva Kanso, and Christophe Eloy. Model of collective fish behavior with hydrodynamic interactions. *Physical review letters*, 120(19):198101, 2018.
- [96] Stephen Childress and Robert Dudley. Transition from ciliary to flapping mode in a swimming mollusc: flapping flight as a bifurcation in re_ω . *Journal of Fluid Mechanics*, 498:257–288, 2004.
- [97] Nicolas Vandenberghe, Stephen Childress, and Jun Zhang. On unidirectional flight of a free flapping wing. *Physics of Fluids*, 18(1):014102, 2006.
- [98] Z Jane Wang. Vortex shedding and frequency selection in flapping flight. *Journal of Fluid Mechanics*, 410:323–341, 2000.
- [99] Shih-Ting Huang. *On the mechanism of forward motion during flapping flight: Numerical simulation by the immersed boundary method*. PhD thesis, New York University, 2007.
- [100] Silas Alben. An implicit method for coupled flow–body dynamics. *Journal of Computational Physics*, 227(10):4912–4933, 2008.
- [101] Jian Deng and Colm-cille Patrick Caulfield. Dependence on aspect ratio of symmetry breaking for oscillating foils: implications for flapping flight. *Journal of Fluid Mechanics*, 787:16–49, 2016.
- [102] Jian Deng and Colm-cille Patrick Caulfield. Horizontal locomotion of a vertically flapping oblate spheroid. *Journal of Fluid Mechanics*, 840:688–708, 2018.
- [103] Brendan J Borrell, Jeremy A Goldbogen, and Robert Dudley. Aquatic wing flapping at low reynolds numbers: swimming kinematics of the antarctic pteropod, *clione antarctica*. *Journal of Experimental Biology*, 208(15):2939–2949, 2005.
- [104] G.K. Batchelor. *An introduction to fluid dynamics*. Cambridge University Press, Cambridge, 1967.
- [105] Hidenori Hasimoto. On the flow of a viscous fluid past a thin screen at small reynolds numbers. *Journal of the Physical Society of Japan*, 13(6):633–639, 1958.
- [106] DB Ingham, T Tang, and BR Morton. Steady two-dimensional flow past a normal flat plate. *Zeitschrift für angewandte Mathematik und Physik ZAMP*, 42(4):584–604, 1991.
- [107] Hidenori Hasimoto. On the periodic fundamental solutions of the stokes equations and their application to viscous flow past a cubic array of spheres. *Journal of Fluid Mechanics*, 5(2):317–328, 1959.
- [108] GK Batchelor. Sedimentation in a dilute dispersion of spheres. *Journal of fluid mechanics*, 52(2):245–268, 1972.
- [109] John F Brady, Ronald J Phillips, Julia C Lester, and Georges Bossis. Dynamic simulation of hydrodynamically interacting suspensions. *Journal of Fluid Mechanics*, 195:257–280, 1988.
- [110] RJ Phillips, JF Brady, and G Bossis. Hydrodynamic transport properties of hard-sphere dispersions. i. suspensions of freely mobile particles. *The Physics of fluids*, 31(12):3462–3472, 1988.
- [111] EJ Hinch. Sedimentation of small particles. In *Disorder and Mixing*, pages 153–162. Springer, 1988.
- [112] James W Swan and John F Brady. Particle motion between parallel walls: Hydrodynamics and simulation. *Physics of Fluids*, 22(10):103301, 2010.
- [113] James W Swan and John F Brady. The hydrodynamics of confined dispersions. *Journal of Fluid Mechanics*, 687:254–299, 2011.

- [114] Elisabeth Guazzelli and John Hinch. Fluctuations and instability in sedimentation. *Annual review of fluid mechanics*, 43:97–116, 2011.
- [115] Ludvig Af Klinteberg and Anna-Karin Tornberg. Fast ewald summation for stokesian particle suspensions. *International Journal for Numerical Methods in Fluids*, 76(10):669–698, 2014.
- [116] Anthony JC Ladd. Numerical simulations of particulate suspensions via a discretized boltzmann equation. part 2. numerical results. *Journal of fluid mechanics*, 271:311–339, 1994.
- [117] Peter J Mucha, Shang-You Tee, David A Weitz, Boris I Shraiman, and Michael P Brenner. A model for velocity fluctuations in sedimentation. *Journal of fluid mechanics*, 501:71–104, 2004.
- [118] Xiaolong Yin and Donald L Koch. Velocity fluctuations and hydrodynamic diffusion in finite-reynolds-number sedimenting suspensions. *Physics of Fluids*, 20(4):043305, 2008.
- [119] Walter Fornari, Mehdi Niazi Ardekani, and Luca Brandt. Clustering and increased settling speed of oblate particles at finite reynolds number. *Journal of Fluid Mechanics*, 848:696–721, 2018.
- [120] Walter Fornari, Francesco Picano, and Luca Brandt. Sedimentation of finite-size spheres in quiescent and turbulent environments. *Journal of Fluid Mechanics*, 788:640–669, 2016.
- [121] Francis H Harlow and J Eddie Welch. Numerical calculation of time-dependent viscous incompressible flow of fluid with free surface. *The physics of fluids*, 8(12):2182–2189, 1965.
- [122] HR Tamaddon-Jahromi, P Townsend, and MF Webster. Unsteady viscous flow past a flat plate orthogonal to the flow. *Computers & fluids*, 23(2):433–446, 1994.
- [123] Subhankar Sen, Sanjay Mittal, and Gautam Biswas. Steady separated flow past a circular cylinder at low reynolds numbers. *Journal of Fluid Mechanics*, 620:89, 2009.
- [124] YF Peng, Amalendu Sau, Robert R Hwang, WC Yang, and Chih-Min Hsieh. Criticality of flow transition behind two side-by-side elliptic cylinders. *Physics of Fluids*, 24(3):034102, 2012.
- [125] Dan Yang, Bjørnar Pettersen, Helge I Andersson, and Vagesh D Narasimhamurthy. Vortex shedding in flow past an inclined flat plate at high incidence. *Physics of fluids*, 24(8):084103, 2012.
- [126] M Cid Montoya, F Nieto, AJ Alvarez, S Hernández, JA Jurado, and R Sánchez. Numerical simulations of the aerodynamic response of circular segments with different corner angles by means of 2d urans. impact of turbulence modeling approaches. *Engineering Applications of Computational Fluid Mechanics*, 12(1):750–779, 2018.
- [127] C. H. K. Williamson. Vortex dynamics in the cylinder wake. *Annu. Rev. Fluid Mech.*, 284:477–539, 1996.
- [128] Daniel Floryan, Tyler Van Buren, and Alexander J Smits. Large-amplitude oscillations of foils for efficient propulsion. *Physical Review Fluids*, 4(9):093102, 2019.
- [129] Wim M Van Rees, Mattia Gazzola, and Petros Koumoutsakos. Optimal morphokinematics for undulatory swimmers at intermediate reynolds numbers. *Journal of Fluid Mechanics*, 775:178–188, 2015.
- [130] M Saadat, Frank E Fish, AG Domel, V Di Santo, GV Lauder, and H Haj-Hariri. On the rules for aquatic locomotion. *Physical Review Fluids*, 2(8):083102, 2017.
- [131] Peter J Schmid, Dan S Henningson, and DF Jankowski. Stability and transition in shear flows. applied mathematical sciences, vol. 142. *Appl. Mech. Rev.*, 55(3):B57–B59, 2002.
- [132] L.A. Miller and C.S. Peskin. When vortices stick: an aerodynamic transition in tiny insect flight. *J. Exp. Biol.*, 207(17):3073–3088, 2004.
- [133] LA Miller and CS Peskin. Flexible clap and fling in tiny insect flight. *The Journal of experimental biology*, 212(19):3076, 2009.

- [134] SK Jones, R Laurenza, Tyson L Hedrick, Boyce Eugene Griffith, and Laura A Miller. Lift vs. drag based mechanisms for vertical force production in the smallest flying insects. *Journal of theoretical biology*, 384:105–120, 2015.
- [135] Arvind Santhanakrishnan, Shannon K Jones, William B Dickson, Martin Peek, Vishwa T Kasoju, Michael H Dickinson, and Laura A Miller. Flow structure and force generation on flapping wings at low reynolds numbers relevant to the flight of tiny insects. *Fluids*, 3(3):45, 2018.
- [136] AN Skipper, DW Murphy, and DR Webster. Characterization of hop-and-sink daphniid locomotion. *Journal of Plankton Research*, 41(2):142–153, 2019.
- [137] Yufeng Chen, Hongqiang Wang, E Farrell Helbling, Noah T Jafferis, Raphael Zufferey, Aaron Ong, Kevin Ma, Nicholas Gravish, Pakpong Chirarattananon, Mirko Kovac, et al. A biologically inspired, flapping-wing, hybrid aerial-aquatic microrobot. *Science Robotics*, 2(11), 2017.
- [138] Jiachen Zhang and Eric Diller. Untethered miniature soft robots: Modeling and design of a millimeter-scale swimming magnetic sheet. *Soft robotics*, 5(6):761–776, 2018.
- [139] Wenqi Hu, Guo Zhan Lum, Massimo Mastrangeli, and Metin Sitti. Small-scale soft-bodied robot with multimodal locomotion. *Nature*, 554(7690):81–85, 2018.
- [140] Ziyu Ren, Wenqi Hu, Xiaoguang Dong, and Metin Sitti. Multi-functional soft-bodied jellyfish-like swimming. *Nature communications*, 10(1):1–12, 2019.
- [141] Yufeng Chen, Huichan Zhao, Jie Mao, Pakpong Chirarattananon, E Farrell Helbling, Nak-seung Patrick Hyun, David R Clarke, and Robert J Wood. Controlled flight of a microrobot powered by soft artificial muscles. *Nature*, 575(7782):324–329, 2019.